1-1-2019

Stress Distortion Restraint to Boost the Sodium Ion Storage Performance of a Novel Binary Hexacyanoferrate

Weijie Li
University of Wollongong, weijie@uow.edu.au

Chao Han
University of Wollongong, chan@uow.edu.au

Wanlin Wang
University of Wollongong, ww268@uowmail.edu.au

Qingbing Xia
University of Wollongong, qx366@uowmail.edu.au

Shulei Chou
University of Wollongong, shulei@uow.edu.au

See next page for additional authors

Stress Distortion Restraint to Boost the Sodium Ion Storage Performance of a Novel Binary Hexacyanoferrate

Abstract

© 2019 WILEY-VCH Verlag GmbH & Co. KGaA, Weinheim Mn-based hexacyanoferrate NaxMnFe(CN)6 (NMHFC) has been attracting more attention as a promising cathode material for sodium ion storage owing to its low cost, environmental friendliness, and its high voltage plateau of 3.6 V, which comes from the Mn2+/Mn3+ redox couple. In particular, the Na-rich NMHFC (x > 1.40) with trigonal phase is considered an attractive candidate due to its large capacity of ≈130 mAh g−1, delivering high energy density. Its unstable cycle life, however, is holding back its practical application due to the dissolution of Mn2+ and the trigonal-cubic phase transition during the charge–discharge process. Here, a novel hexacyanoferrate (Na1.60Mn0.833Fe0.167[Fe(CN)6], NMFHFC-1) with Na-rich cubic structure and dual-metal active redox couples is developed for the first time. Through multiple structural modulation, the stress distortion is minimized by restraining Mn2+ dissolution and the trigonal-cubic phase transition, which are common issues in manganese-based hexacyanoferrate. Moreover, NMFHFC-1 simultaneously retains an abundance of Na ions in the framework. As a result, Na1.60Mn0.833Fe0.167[Fe(CN)6] electrode delivers high energy density (436 Wh kg−1) and excellent cycle life (80.2% capacity retention over 300 cycles), paving the way for the development of novel commercial cathode materials for sodium ion storage.

Disciplines

Engineering | Physical Sciences and Mathematics

Publication Details

Li, W., Han, C., Wang, W., Xia, Q., Chou, S., Gu, Q., Johannessen, B., Liu, H. & Dou, S. (2019). Stress Distortion Restraint to Boost the Sodium Ion Storage Performance of a Novel Binary Hexacyanoferrate. Advanced Energy Materials,

Authors

Weijie Li, Chao Han, Wanlin Wang, Qingbing Xia, Shulei Chou, Qinfen Gu, Bernt Johannessen, Hua-Kun Liu, and Shi Xue Dou

Stress distortion restraint to boost the sodium ion storage performance of a novel binary hexacyanoferrate

Weijie Li,[a] Chao Han,[a] Wanlin Wang,[a] Qingbing Xia,[a] Shulei Chou,[a] Qinfen Gu,[b*] Bernt Johannessen,[b] HuaKun Liu,[a] Shixue Dou[a]*

[a]Dr. W. Li, Dr. C. Han, W. Wang, Q. Xia, Dr. S. Chou, Prof. H. Liu and Prof. S. Dou
Institute for Superconducting and Electronic Materials, University of Wollongong.
Wollongong, NSW 2522 Australia
E-mail: shulei@uow.edu.au

[b]Dr. Q. Gu, B. Johannessen
Australian Synchrotron (ANSTO), 800 Blackburn Rd, Clayton 3168, Australia.
E-mail: qinfeng@ansto.gov.au

Keywords: binary hexacyanoferrate, sodium-rich cubic phase, no phase transformation, Mn dissolution-free, minimized structural strain

Mn-based hexacyanoferrate $Na_xMnFe(CN)_6$ (NMHFC) has been attracting more attention as a promising cathode material for sodium ion storage owing to its low cost, environmental friendliness, and even its high voltage plateau of 3.6 V, which comes from the Mn^{2+}/Mn^{3+} redox couple. In particular, the Na-rich NMHFC (x > 1.40) with trigonal phase is considered as an attractive candidate due to its large capacity of ~130 mAh g^{-1}, delivering high energy density. Its unstable cycle life, however, is holding back its practical application due to the dissolution of Mn^{2+} and the trigonal-cubic phase transition during the charge-discharge process. Here, a novel hexacyanoferrate ($Na_{1.60}Mn_{0.833}Fe_{0.167}[Fe(CN)_6]$, NMFHFC) with Na-rich cubic structure and dual-metal active redox couples is developed for the first time. Through multiple structural modulation, the stress distortion is minimized by restraining Mn^{2+} dissolution and the trigonal-cubic phase transition, which are common issues in manganese-based hexacyanoferrate. Moreover, NMFHFC simultaneously retains an abundance of Na ions in the framework. As a result, $Na_{1.60}Mn_{0.833}Fe_{0.167}[Fe(CN)_6]$ electrode delivers high energy density (436 Wh kg^{-1}) and excellent cycle life (80.2% capacity retention over 300 cycles), paving the way for the development of novel commercial cathode materials for sodium ion storage.

1. Introduction

Due to the exhaustion of fossil fuels and environmental pollution, the utilization of renewable energy has become imperative. Renewable forms of energy, such as wind and solar energy, however, are intermittent due to weather variation. To store these sorts of renewable energy, a large amount of rechargeable battery capacity is needed. Owing to the low cost and abundant resources of sodium, sodium ion batteries (SIBs) have attracted considerable attention in the past ten years and are considered as a new generation of energy storage devices to replace lithium ion batteries (LIBs) in certain applications.[1-11] Hitherto, the commercialization of SIBs has been held back, however, by their low energy density and unsatisfactory cycle life. The cathode, as much as the anode, also plays an important role in the final performance of the battery. Thus, it is crucial to develop cathode candidates with both high energy density and stable cycle life for sodium ion storage.

It is accepted that the energy density is determined by the specific capacity and the voltage plateau of an electrode. The commercial cathode materials for LIBs can deliver 510-700 Wh/kg energy density with a potential plateau of 3.4-4.1 V (3.4 V for $LiFePO_4$, 4.1 V for spinel $LiMn_2O_4$) and high specific capacity of over 150 mAh g^{-1}. In comparison, most of the cathode candidates reported for SIBs show a potential plateau below 3.2 V and a capacity below 110 mAh g^{-1}, delivering energy density lower than 350 Wh kg^{-1}.[12-17] Exceptionally, the sodium superionic conductor (NASICON) $Na_3V_2(PO_4)_3$ presented a 3.4 V potential plateau and 115 mAh g^{-1} capacity; $Na_3(VO_{1-x}PO_4)_2F_{1+2x}$ ($0 < x < 1$) showed 3.8-3.9 V average voltage and 120-130 mAh g^{-1} capacity.[18-22] Honeycomb-layered $Na_3Ni_2SbO_6$ provided an average working potential at 3.3 V and a high capacity of ~120 mAh g^{-1}. Moreover, $Na_3Ni_2SbO_6$ showed superior rate capability and excellent cycling performance.[23-24] In the long run, however, these cathode materials containing toxic elements (V and Sb) are not suitable for commercial SIBs, because commercialization also requires electrode materials to possess the properties of environmental friendliness and low cost in addition to excellent electrochemical performance.

Recently, Prussian blue analogues (PBAs) have attracted much attention owing to their low cost and environmental-friendliness.[6, 25-28] The PBAs utilized for electrode materials can be classified into 3 groups, that is, hexacyanoferrates ($ATFe(CN)_6$), hexacyanomanganates ($ATMn(CN)_6$) and hexacyanocobaltates ($ATCo(CN)_6$, where A = K, Na; T = Fe, Mn, Ni, Co). Among them, hexacyanoferrates, in particular, have been put under the spotlight due to their non-poisonous raw material ferrocyanide ($Na_4Fe(CN)_6$ or $K_3Fe(CN)_6$), while the raw materials $K_3Mn(CN)_6$ for hexacyanomanganate and $K_3Co(CN)_6$ for hexacyanocobaltate are harmful and toxic. In the case of hexacyanoferrates, the ones containing the abundant and non-toxic elements Fe and Mn are attractive for potential commercial SIBs. The Fe-based hexacyanoferrate $Na_xFeFe(CN)_6$ has shown excellent stable cycle life, but it presents both a low voltage plateau at 3.0 V and low capacity around 100 mAh g^{-1}. Although the capacity was improved to ~115 mAh g^{-1} by substituting sodium ions for crystal water in the framework,[26, 29] the voltage plateau is still low at 3.0 V owing to the intrinsic properties of the Fe^{2+}/Fe^{3+} redox couple. Moreover, the synthetic method used is a semi-hydrothermal method, which is not suitable for commercial application due to low product yield. In contrast, the Mn-based hexacyanoferrate $Na_xMnFe(CN)_6$ (NMHFC) showed a high voltage plateau of 3.6 V coming from the Mn^{2+}/Mn^{3+} redox couple. The Na-rich NMHFC ($x > 1.40$) shows an especially high energy density with large capacity of 125 mAh g^{-1}. Its cycle life, however, is not stable due to the dissolution of Mn^{2+} and its trigonal-cubic phase transition.[28, 30] One hypothesis is proposed, that the $Na_xMnFe(CN)_6$ framework could be stabilized and that the compound could simultaneously possess a higher voltage plateau if the Mn^{2+} could be selectively removed while maintaining the Mn^{3+} via introducing a second transition metal (T, T = Fe, Co, Ni, Cu, V; $0 < x < 1$). Moreover, the dual active redox sites of T and Mn could endow the framework with superior properties in comparison with the traditional PBA framework possessing a single active redox site.

Herein, a series of binary hexacyanoferrates with the formula $Na_xFe_yMn_{1-y}Fe(CN)_6$ (denoted as NMFHFC, $0 < x < 2$, $0 < y < 1$) have been synthesized and their electrochemical performance tested as cathodes for sodium-ion storage for the first time, with special consideration of their environmental friendliness (Fe and Mn elements) and commercial prospects. In this work, the Fe/Mn-based binary hexacyanoferrate NMFHFC has been developed through a facile and energy-efficient co-precipitation method for the first time. Moreover, NMFHFC presents sodium-rich cubic phase and the substitution of Fe for dissoluble Mn^{2+}, resulting in avoidance of the stress distortion due to Mn^{2+} dissolution and the rhombohedral-cubic phase transition. As a result, $Na_{1.60}Mn_{0.833}Fe_{0.167}[Fe(CN)_6]$ delivered high capacity of 123 mAh g^{-1} and excellent cycle life, with 80.2% capacity retention over 300 cycles. Notably, NMFHFC can be easily synthesized on a kilogram scale due to its facile synthesis method. This work provides a new strategy to develop new promising cathode candidates for commercial SIBs.

2. Results and discussions

2.1. Structure characterization

The Fe/Mn-based binary hexacynoferrate NMFHFC samples were prepared by a facile co-precipitation method, where a solution of Fe- and Mn-salts is added into a solution of $Na_4Fe(CN)_6$. The details are described in the experimental section. To explore the structure of NMFHFC, the as-prepared NMFHFC samples were investigated by synchrotron X-ray powder diffraction (XRPD), and structures were refined by the Rietveld method. Figure 1(a) shows the synchrotron XRPD pattern and refinement plot of the sample NMFHFC-1. NMFHFC-1 exhibited a single phase with all peaks fitted, and it had a face-centred-cubic (fcc) structure with the lattice parameters $a = b = c = 10.515(1)$ Å in space group F*m*-*3m*. Moreover, both the energy dispersive spectroscopy (EDS) and inductively coupled plasma (ICP) results on NMFHFC-1 show that the Fe content is higher than that of Mn in the sample (Tables S1 and S2 in the Supporting Information), demonstrating that the Fe/Mn-based binary hexacyanoferrates

$Na_xFe_yMn_{1-y}Fe(CN)_6$ had been successfully synthesized. According to the ICP results, the formula for the NMFHFC-1 sample is $Na_{1.60}Mn_{0.833}Fe_{0.167}[Fe(CN)_6]$, suggesting that Na-rich cubic phase was obtained. Interestingly, using the same synthesis method, the pure Mn-based hexacyanoferrate (NMHFC) showed the trigonal structure with $a = b = 7.539(1)$ Å, $c = 17.9193(1)$ Å in space group R-3 from the refined XRPD data in Figure 1(b).

According to the refined crystallographic data, Na atoms in NMHFC occupy the 6*c* positions in the voids of the structure and deviate towards Mn atoms of the $MnFe(CN)_6$ framework, while the Na atoms in NMFHFC occupy 8*c* positions in the middle of the voids in the $Fe_yMn_{1-y}Fe(CN)_6$ framework (Figure 1(c-d)). In addition, the Fe atoms are coordinated with C, and the Mn atoms are coordinated with N in the framework of NMHFC. In comparison, in the NMFHFC framework, the transition metal (T) sites coordinated with N are occupied by a mixed occupancy of Mn and Fe atoms (Figure 1(c)), with a unit cell having right angles as compared with a slightly distorted 91.3° in the trigonal structure of NMHFC. Thus, it is deduced that the binary hexacyanoferrate NMFHFCs are solid solution of hexacyanometalates, where Fe atoms partially replace the nitrogen-coordinated Mn atoms in the framework. This is consistent with a report in which nitrogen-coordinated metal ions were substituted into solid solutions of hexacyanometalates.[31]

It is thus demonstrated that the trigonal structure can be tuned to the cubic phase after the introduction of the second electrochemically active Fe ion into the NMHFC structure, which will be further discussed with the density functional theory (DFT) calculation results. A series of NMFHFC samples ($Na_xFe_yMn_{1-y}Fe(CN)_6$, $y = 0$, 1/6, 1/3, 1/2, 2/3) with different amounts of active Fe were prepared. Notably, the diffraction peaks of the NMFHFC samples were shifted to higher angles, suggesting that the lattice parameters decreased with an increasing amount of active Fe in the NMFHFC framework (Figure S1). The structural details of the NMFHFC samples were further explored by synchrotron X-ray powder diffraction (XRPD) and refined

by the Rietveld method, as shown in Figure S2. All the NMFHFC samples present fcc structures. NMFHFC-2 showed a smaller lattice parameter (10.486(1) Å) than that of NMFHFC-1 (10.515(1) Å), resulting from more Fe with a smaller ionic radius substituting for Mn in the framework. When the amount of active Fe was increased to 1/2 and 2/3, a second set of diffraction peaks was observed as a second phase with slightly different lattice parameters, which appears in the NMFHFC-3 and NMFHFC-4 samples, respectively (Figure S2). The lattice parameters of the NMFHFC samples are listed in Tables S3-S8. It is clearly observed that the lattice parameters continuously decrease from the NMFHFC-1 to the NMFHFC-4 sample. The morphologies of the NMFHFC samples were observed by scanning electron microscopy (SEM). It is clear that the NMFHFC samples presents granular-like particles with sizes of 80-100 nm, as shown in Figure S3. Moreover, the Fe/Mn-based binary hexacyanoferrate NMFHFC samples are easy to scale up because the synthetic method is easy and productive (Figure S4).

To further explore the structural details of the NMFHFC samples, various characterization techniques, including Mössbauer spectroscopy, Raman spectroscopy, thermogravimetric analysis (TGA), and investigations on a physical properties measurement system (PPMS), were carried out, and the results are shown in Figure 2. Mössbauer spectroscopy was carried out to detect the valence state of Fe in the NMFHFC samples, and the results are shown in Figure 2(a), with the occupancies of Fe^{2+} and Fe^{3+} listed in Table S9. As shown in Figure 2(a), Fe^{2+} ions only exist in the form of $Fe(CN)_6^-$ in pristine NMHFC. In comparison, the Fe/Mn-based binary hexacynoferrate NMFHFC samples have both Fe^{3+} and Fe^{2+}. Moreover, with increasing amounts of active Fe in the NMFHFC framework, the proportion of Fe^{3+} in the NMFHFC framework rises, from 23.9% for NMFHFC-1 up to 50.5% for NMFHFC-4, while the percentage of Fe^{2+} changed in the reverse way, decreasing from 76.1% for NMFHFC-1 to 49.5% for NMFHFC-4 (Table S9). This demonstrates that the introduced Fe exists mainly in the form of Fe^{3+} in the NMFHFC framework.

To verify this result, Raman spectra were collected to determine the valence states of transition metal ions bonded to CN^- groups. Figure 2(b) presents the Raman spectra of the NMFHFC samples and NMHFC sample. Clearly, some peaks were observed in the range of 2050-2200 cm^{-1}, which were assigned to the CN^- groups, demonstrating that the transition-metal ions bonded to the CN^- groups exhibit different valence states. The primary NMHFC sample showed two peaks at 2083.5 cm^{-1} and 2131.8 cm^{-1}, corresponding to Fe^{2+}-CN-Mn^{2+} and Fe^{2+}-CN-Mn^{3+}, respectively. In comparison, the Raman spectrum of the NMFHFC-1 sample presented two main peaks at 2110.5 cm^{-1} and 2137.3 cm^{-1}, which were assigned to Fe^{2+}-CN-Fe^{3+} and Fe^{2+}-CN-Mn^{3+}, respectively. In addition, there is a weak peak observed at 2061.6 cm^{-1} that is related to Fe^{2+}-CN-Fe^{2+}. The peak positions of the Raman spectra are listed in Table S10. Notably, on increasing the amount of active Fe, the Raman peaks of NMFHFC shifted to higher wavenumber, indicating that the average valence state of the transition metals was raised along with the amount of active Fe in the NMFHFC samples.[30] In addition, the X-ray photoelectron spectroscopy (XPS) spectra show that the binding energy of the Fe $2p_{3/2}$ spectrum shifts from 708.7 eV to the higher value of 709.8 eV, and the Mn $2p_{3/2}$ spectrum also shifts slightly to the right, suggesting that the average valence states of Fe and Mn increase after the second metal ion is introduced into framework (Figure S5, Supporting Information). Electron energy-loss spectroscopy (EELS) was carried out to explore the valences of Mn and Fe for the NMFHFC-1 sample. Figure 2(c) shows the Mn $L_{3,2}$ and Fe $L_{3,2}$ white lines obtained from several NMFHFC-1 particles. The shapes of the $MnL_{2,3}$ white lines show symmetric peaks (Mn L_3 at 643.2 eV), and the intensity ratio of L_3/L_2 is 2.42, suggesting that the Mn element exists in the single oxidation state of Mn^{3+}. The X-ray absorption near-edge spectroscopy (XANES) results further verify that Mn in the NMFHFC-1 sample exhibits a similar adsorption edge to that of Mn_2O_3 (Figure S6), suggesting that the oxidation state of Mn is 3+.[32] In contrast, the Fe $L_{2,3}$ white lines represent asymmetric peaks, in which Fe L_3 is fitted into two peaks at 707.6 eV and 710.5 eV. Moreover, the intensity ratio of Fe L_3/L_2 is 4.61, demonstrating that the oxidation

states of Fe involve Fe^{2+} and Fe^{3+}, respectively.[33] Given the results from analysis of Raman, EELS, and XPS spectra, and the XANES patterns, it is manifest that Mn element in the NMFHFC samples is only present in the Mn^{3+} state, while Fe presents in both Fe^{2+} and Fe^{3+} states, with some amount of Fe substitution for Mn in the NMFHFC framework.

To verify the water content in the NMFHFC samples, thermogravimetric analysis (TGA) was carried out in argon from 50 to 500℃ at the heating rate of 5℃/min, as shown in Figure 2(d). The weight loss at < 120℃ was assigned to evaporation of the adsorbed water on the particle surfaces, while the weight loss in the temperature range of 120-200℃ can be related to the elimination of zeolitic water in the structure, which determines the water content on a per formula basis.[34] Compared to NMHFC (9.15 wt%), the water content of the NMFHFC samples is reduced significantly, with 4.71%, 5.38%, 5.68%, and 5.94% for NMFHFC-1, NMFHFC-2, NMFHFC-3, and NMFHFC-4, respectively. To understand the dehydration behaviour of NMFHFC and NMHFC samples, in-situ high temperature synchrotron XRPD was conducted from 30°C to 300°C, and the results are shown in Figure 2(g-h). NMHFC sample shows trigonal structure at 30°C, and shows a gradually phase transformation to cubic structure from 90°C and complete at 130°C. The cubic phase starts decomposition from 230°C. In contrast, NMFHFC-1 sample shows a cubic structure from 30°C up to 260°C, then it starts decomposition from 270°C. Combined with TGA results, it indicates that the Fe-substitution not only decrease the water content but also improve the thermal stability of Mn-based hexacyanoferrate.

To further identify the valence and spin states of Fe and Mn in the NMFHFC samples, the temperature dependence of the magnetic susceptibility (χ) of the NMFHFC powders was determined, as shown in Figure 2(e-f). All the NMFHFC powders exhibit paramagnetic behaviour at low temperature, and there is no phase transition observed in this temperature range (Figure 2(e)). The calculated effective magnetic moments (μ_{eff}) of NMHFC, NMFHFC-

1, NMFHFC-2, NMFHFC-3, and NMFHFC-4 are 4.09 μ_B, 4.13 μ_B, 4.14 μ_B, 4.11 μ_B, and 4.10 μ_B per formula unit, respectively. Based on the XPS, EELS and Raman results, Fe ions coordinated by C are Fe^{2+}, while the metal ions coordinated by N are in the Fe^{3+}, Fe^{2+}, and Mn^{3+} states in the NMFHFC samples. In contrast, the Mn ions coordinated by N are in the Mn^{2+} and Mn^{3+} states in the NMHFC sample. The Fe ions coordinated by C are in the low-spin state, while the Mn (or substituted Fe) ions coordinated by N are in the high-spin state.[30] Moreover, the effective magnetic moment for the low-spin state of Fe^{2+} (S = 0) is 0 μ_B, while those for the high-spin states of Mn^{2+} (S = 5/2), Mn^{3+} (S = 2), Fe^{2+} (S = 2), and Fe^{3+} (S = 5/2) are 5.92 μ_B, 4.90 μ_B, 4.90 μ_B, and 5.92 μ_B, respectively. The calculated effective magnetic moments of all the NMFHFC samples remained at the same level and only changed a little with the introduction of the secondary Fe element into the framework, demonstrating that the spin-state of the transition metal shows almost no change.

2.2. Electrochemical performance evaluation

The electrochemical performances of the NMFHFC composites were evaluated in coin cells with Na foil used as the counter electrode. The cells were tested in an electrolyte composed of 1 M $NaClO_4$ in ethylene carbonate (EC) and diethyl carbonate (DEC) in the voltage range of 2.0-4.2 V (versus Na^+/Na). Figure 3a shows the first five charge-discharge curves of NMFHFC-1 composite at a current density of 0.1 C, corresponding to 10 mA g^{-1}. NMFHFC-1 delivered a discharge capacity of 123 mAh g^{-1} in the first cycle, with an initial coulombic efficiency of 91.7%. Compared with $Na_xMnFe(CN)_6$ with no active Fe in manganese sites (72.6% initial coulombic efficiency), NMFHFC-1 presents a relatively high initial coulombic efficiency, owing to the lesser amount of zeolitic water in the structure (Figure S8), which will be removed irreversibly during the initial charge process.[28] In order to avoid disturbance of the amount of zeolite water, the electrochemical performance of the dehydrated NMHFC and NMFHFC-1 samples were evaluated. NMFHFC-1 dehydrated at 180° C still presents the more stable cycling

performance than that of NMHFC (Figure S8). Combining with the in-situ high temperature synchrotron XRPD (Figure 2g-h), it demonstrates that the Fe-substitution improving NMHFC the thermal and cycling stability. The NMFHFC-1 shows an average voltage potential of 3.55 V, delivering an energy density of ~ 436 Wh kg^{-1}. There are three voltage regions in the discharge curves of NMFHFC-1: 1) region I is located between 4.2-3.55 V, corresponding to the redox couple of the high-spin $Mn^{2+/3+}$ coordinated with N;[30] 2) voltage region Π is at 3.55-3.08 V, assigned to the redox couple of low-spin $Fe^{2+/3+}$ coordinated with C; [30] and 3) voltage region Ш at 3.08-2.0 V is related to the high-spin $Fe^{2+/3+}$ coordinated with N.[26]

To compare the electrochemical performances of the NMFHFC samples more clearly, the initial charge-discharge curves of the NMFHFC samples are plotted in Figure 3b. The open circuit voltage (OCV) values for the NMFHFC-1, NMFHFC-2, NMFHFC-3, and NMFHFC-4 samples are 3.0 V, 3.02 V, 3.06 V, and 3.09 V, respectively. It is clear that the OCV value rises as the amount of active Fe increases in the NMFHFC samples, suggesting that the average valence of metal ions has increased in the NMFHFC framework, owing to the dependence of the OCV of NMFHFC samples on the valence state of the metal ions.[30] This indication is consistent with the Raman and XPS results. Correspondingly, the initial charge capacity becomes smaller with the rise of OCV values, due to fewer Na ions in the framework for the charge, which corresponds to the increasing average valence of the metal ions. The EDS and ICP results also show the same tendency, that the sodium content in NMFHFC samples is reduced as the amount of Fe increases (Tables S1, S2). The overpotential of the charge-discharge curve for NMFHFC-1 is relatively low, about 0.32 V, while the overpotentials for NMFHFC-2, NMFHFC-3, and NMFHFC-4 are 0.41 V, 0.49 V, and 0.53 V, respectively.

Three voltage plateaus are clearly observed during the charge (3.02, 3.52, and 3.85 V) and discharge (2.75, 3.27, and 3.57 V) in the first cycle for all the NMFHFC samples, as shown in Figure 3b. It is notable that the part of the charge-discharge curve related to the redox couple of $Mn^{3+/2+}$ gradually becomes shorter when the amount of active Fe is increased in the

NMFHFC samples. In contrast, the one assigned to the redox couple of high-spin $Fe^{3+/2+}$ becomes longer. Additionally, the capacity contributed by the low-spin $Fe^{2+/3+}$ coordinated with C (Fe in $Fe(CN)_6^{4-}$) becomes smaller as the amount of active-Fe increases in the NMFHFC framework, indicating that the content of $Fe(CN)_6^{4-}$ groups in the framework is decreasing and the amount of defects/vacancies is increasing. As a result, the greater density of vacancies existing in the framework makes the discharge capacity continually decrease from 122.7 mAh g^{-1} for NMFHFC-1 to 110.8 mAh g^{-1} for the NMFHFC-4 sample (Figure 3b).

Figure 3c presents cyclic voltammetry (CV) curves of the NMFHFC samples. The CV curve of NMFHFC-1 shows two pairs of the dominant anodic/cathodic peaks centred at 3.54 V/3.22 V and 3.74 V/3.34 V, corresponding to the redox couple of the low-spin Fe^{2+}/Fe^{3+} and the high-spin Mn^{2+}/Mn^{3+}, respectively.[30] Moreover, a small anodic peak at ~ 3.01 V is observed, assigned to the oxidation of the high-spin Fe^{2+}.[26] In the case of the NMFHFC-4 sample, there are two pairs of the main redox peaks at 3.69 V/3.16 V and 3.10 V/2.78 V, assigned to the high-spin Mn^{2+}/Mn^{3+} and Fe^{2+}/Fe^{3+}, respectively. Due to the lower amount of $Fe(CN)_6^{4-}$ in NMFHFC-4, the corresponding redox peaks at higher voltage of 3.74 V/3.34 V are difficult to distinguish in the CV curve. In contrast, these three couples of the redox peaks are obviously observed in the NMFHFC-2 and NMFHFC-3 compounds. As the amount of Fe-doping increased, the intensity of the redox peaks related to the low-spin Fe coordinated by C in $Fe(CN)_6^{4-}$ (at 3.5 V) obviously decreased, while that of peaks assigned to the high-spin Fe (at 3.07 V/2.74 V) increased, demonstrating that the amount of low-spin Fe decreased, whereas the amount of high-spin Fe increased in line with the charge-discharge curves.

Figure 3d shows the rate capability of the NMFHFC samples at various rates from 0.1 C – 20 C. NMFHFC-1 exhibited superior rate capability compared with the other NMFHFC samples, delivering the high capacity of 80.6, 62.9, 47.1, and 21.0 mAh g^{-1} even at the high rate of 2 C, 5 C, 10 C, and 20 C, respectively. To explain the superior rate capability of NMFHFC-1, electrochemical impedance spectroscopy (EIS) was carried out. Figure S10a (Supporting

Information) presents the impedance curves of the NMFHFC samples. The EIS curves show a semicircle and an oblique line in the medium-frequency range and the low-frequency range, respectively. According to the equivalent circuit (Figure S10b), the EIS curves can be fitted into two semicircles at high-frequency and medium-frequency, corresponding to the cell internal resistance (R_s) and the charge transfer resistance (R_{ct}), respectively. Clearly, NMFHFC-1 has the smallest R_{ct} of 74.7 Ω (297.3 Ω, 348.9 Ω, and 402.8 Ω for NMFHFC-2, NMFHFC-3, and NMFHFC-4, respectively), demonstrating that its electronic conductivity is better than those of the other samples. In addition, the diffusion dynamics of the NMFHFC samples was investigated by the galvanostatic intermittent titration technique (GITT) and cyclic voltammetry (CV), and the details of the diffusion coefficient calculation are presented in Figures S11-S17 (Supporting Information). The NMFHFC-1 shows the largest diffusion coefficient among all the NMFHFC samples (Figure S15 and Figure S17). The analysis of the EIS, GITT, and CV results explains why the NMFHFC-1 sample has superior rate capability compared to the other NMFHFC samples.

To evaluate the cycling stability of the NMFHFC samples, the cycling performance of the NMFHFC and the pristine NMHFC samples was tested at the 0.2 C rate in the voltage range of 2.0 -4.2 V, and the results are exhibited in Figure 3e. In comparison with the NMHFC sample, the cycling stability of the NMFHFC samples has been significantly improved due to the Fe substitution for the dissoluble Mn in the framework. The NMFHFC-1 and NMFHFC-2 samples present superior cycling stability, with capacity retention of 80.2% and 70.2%, respectively, after 300 cycles. The charge-discharge curves of NMFHFC-1 after 300 cycles are shown in Figure S18. Even after cycling for 1000 cycles at the 1 C rate, the NMFHFC-1 sample shows excellent capacity retention of 62.0% (Figure S19). Compared with the other reported Mn-based hexacyanoferrates, NMFHFC-1 also exhibited superior cycling stability (Table S11). This is possibly due to the Fe substitution for the dissoluble Mn^{2+} in the framework. The cycled NMFHFC-1 cell was examined to explore whether dissolution of Mn occurred during the

cycling process. Figure S20 shows a photograph and the EDS elemental analysis of the separator obtained from the NMFHFC-1 cell after 100 cycles. It is obvious that the colour of the separator did not change after cycling, and no Mn signal was detected in the EDS element analysis, demonstrating that the NMFHFC-1 sample does not undergo dissolution of Mn during the cycling process. In addition, the composition of the cycled NMFHFC-1 electrode was also tested by EDS, and the results are listed in Table S12. The contents of Na and Mn are nearly same as in the as-prepared NMFHFC-1 (Tables S1, S2), while the NMHFC presents the reduced contents of Na and Mn. It suggests the good structural stability of NMFHFC-1 after Fe substitution in NMHFC. Moreover, NMFHFC-1 has good storage stability under ambient atmosphere, with no phase or composition changes after storage under air for 2 years (Figure S21 and Table S13). This advantage endows the NMFHFC sample with promising prospects for commercialization in comparison with the layered metal oxides, most of which are not stable under air. Furthermore, the full-cell performance of NFMHFC-1 was evaluated with commercial hard carbon electrode as anode, and the results are shown in Figure S22. The capacity ratio of cathode/anode is 1.1:1, and the capacity of the full cell is calculated on the basis of cathode mass. The NFMHFC-1/hard carbon cell delivers an initial capacity of 79.8 mAh g^{-1}, with the potential plateau at 3.0 V. The cycling stability is not ideal, with capacity retention of 59.6% over 100 cycles. This is possibly due to the relatively low initial coulombic efficiency of hard carbon and improper capacity matching. Further work will be carried out to optimize the cathode/anode capacity matching and improve the initial coulombic efficiency of the anode.

To further confirm the effects of introduced Fe on the electrochemical performance of hexacyanoferrate, a control sample was prepared (blended NMFHFC, denoted as B-NMFHFC), prepared by mixing the pure Mn-based and Fe-based hexacyanoferrates together in the same ratio of Mn/Fe as that in NMFHFC-1. The electrochemical performance of B-NMFHFC was tested in half-cells, and the results are shown in Figure S23. It is clear that the charge-discharge

curves of B-NMFHFC are different from those of NMFHFC, even though both of them have the same ratio of Mn/Fe. Moreover, the cycling performance of B-NMFHFC is inferior to that of NMFHFC-1. This further demonstrates that NMFHFC-1 is a single phase, in which the structure is stabilized by introducing Fe into the framework.

2.3. Theoretical calculation

In order to understand the Fe doping effects on the PBAs, the variations in NMHFC and NMFHFC samples and their reaction mechanisms were further investigated by DFT calculations. The calculated NMHFC sample with chemical composition of $Na_2MnFe(CN)_6$ (100% Na, 100 at.% Mn in 3*b* sites) indicates that the structure is more stable in the trigonal configuration with the R-3 space group, as it has lower formation energy, as shown in Figure. 4(a). When 50% of Na ions are extracted from the voids in the structure during the charge process, the trigonal structure still shows favourable formation energy for the chemical formula of $Na_1MnFe(CN)_6$. With further extraction of Na ions (0-50 % Na) from the structure during charging, however, the fcc cubic structure shows lower energy compared with the trigonal structure, which indicates a phase transformation between the two structures. This result is in good agreement with our synchrotron XRPD observations indicating a trigonal-cubic structural change of the NMHFC sample in the charge process.[28] Interestingly, with Fe partially replacing Mn in the NMFHFC samples (50 at.% Mn), the cubic structure with 50 % Na ions shows a similar total energy compared with the trigonal structure. Further reducing the Mn content in the PBA framework leads to a lower total energy of the cubic structure compared with the trigonal structure, which indicates that Fe atoms substituted into the framework can stabilize the cubic structure of PBAs, which is consistent with our synthesis results on cubic Na-rich NMFHFC-1. Figure 4(c, d*)* presents the total energy 2D surface plots as functions of Na and Mn contents for the cubic and trigonal structures of PBAs, respectively. Our calculation results demonstrate that both structures become more stable with higher Na and Mn contents in the same crystal structure system. This can explain why the NMFHFC-1 presented the best

cycling performance among the NMFHFC samples. Furthermore, the NMFHFC sample (50 Mn at.%) showed much less volume change (~8%) than the NMHFC sample (100 Mn at.%) with about 12 % volume change during a full charge (100% to 0 % Na) as shown in Figure 4(b). This minimized volume contraction/expansion, inducing negligible structural strain in the battery cycling, and consequently, tNMFHFC-1 remained intact, and its electrodes retained high cycling stability.

2.4. Investigation on storage mechanism

To explore the structural evolution of NMFHFC during the charge-discharge progress, in-situ synchrotron XRPD measurements were carried out on the NMFHFC-1 sample assembled into a modified half-cell. In addition, in-situ X-ray absorption near edge spectroscopy (XANES) and ex-situ XANES were conducted at the Fe K-edge and Mn K-edge on the NMHFC sample to determine the evolution of the metal oxidation states in the batteries. Figure 5(a) shows the in-situ XRPD patterns of NMFHFC-1 during the first charge and discharge process at the current density of 20 mA g^{-1} in the voltage range of 2.0-4.0 V. The main strong peaks of the (002), (022), and (004) planes were selected for investigation. The positions of these peaks shifted right to larger 2θ angles, their peak intensities became weaker, and their peak full width at half maximum (FWHM) values became bigger as the charge process proceeded, demonstrating the contraction of the unit cell and internal structural strain during the sodium-ion extraction from the NMFHFC-1 framework. At the end of the charge process, the (002) peak split into two peaks, and the (022) and (004) peaks were barely observed, owing to the slight contraction of the sodium-deficient NMFHFC-1 crystal structure during the charge process. Such a phenomenon was also observed in the $Na_{1.56}FeFe(CN)_6$ structure.[26] At the onset of the discharge process, the (002), (022), and (004) peaks begin to be restored as sharp symmetrical peaks with the sodium-ion insertion back into the framework. In addition, these peaks gradually shift to lower 2θ values and are nearly restored to their pristine positions (e.g., 2θ of 8.44º compared with the initial one of 8.42º) at the end of the first discharge process. This indicates

the structural integrity and durability of NMFHFC-1 after cycling, which can explain the excellent cycling stability of NMFHFC-1. To determine the evolution of the $[Fe(CN)_6]$ group during the charge-discharge process, the NMHFC-1 sample was chosen for investigation to collect in-situ XANES data at the Fe K-edge. Figure 5(c) shows the normalized Fe K-edge XANES spectra collected during the first discharge process. The Fe K-edge gradually shifted right with more Na-ion extraction from the framework, demonstrating that the Fe^{2+} was oxidized to the Fe^{3+} state. Subsequently, the Fe K-edge gently shifted to the left and back to 7129.3 eV, suggesting the Fe^{3+} was reduced to Fe^{2+} when some Na-ions were intercalated into the framework during the discharge process. In contrast, the Mn K-edge XANES spectrum presents no obvious edge shift after cycling, demonstrating that the Mn oxidation state does not change after electrochemical reaction (Figure S6). It was concluded that $[Fe(CN)_6]$ groups took apart in the electrochemical reaction during the charge-discharge process with the redox couple of $Fe^{2+/3+}$.

Therefore, there are two key factors that can explain the superior cycling performance of NMFHFC-1 compared to the pristine NMHFC, as shown in Figure 6. In the case of pristine NMHFC, it shows the trigonal structure, which undergoes a phase transition from trigonal structure to cubic structure, resulting in distinct lattice distortion, large volume changes, and structural strain during the charge-discharge process. Moreover, the element Mn in NMHFC is present in two forms, Mn^{2+} and Mn^{3+}, in which Mn^{2+} is not stable and can dissolve in the electrolyte. Both phenomena contributed to the unstable structure of NMHFC during cycling. In contrast, with the introduction of secondary Fe, NMFHFC-1 exhibits the cubic structure, and remains in the cubic structure during the charge-discharge process with smaller volume change. In addition, owing to the Fe substitution for part of the Mn, the absence of Mn^{2+} in NMFHFC-1 avoids the dissolution of Mn^{2+} into the electrolyte. The absence of both a phase transformation and Mn^{2+} dissolution is beneficial to the stable cycling performance of NMFHFC-1.

3. Conclusion

In summary, cubic Na-rich $Na_xMn_{1-y}Fe_y[Fe(CN)_6]$ (NMFHFC, $0 < x < 2$, $0 < y < 1$) samples with dual-active sites were prepared by a promising co-precipitation method. The substitution of Fe for Mn eliminates the dissolution of Mn^{2+} ions in the NMFHFC framework, thus stabilizing the structure. In addition, the cubic phase of $Na_xMn_{1-y}Fe_y[Fe(CN)_6]$ shows negligible structural strain during charge-discharge processes owing to the avoidance of the trigonal-cubic phase transition that is observed in the pristine $NaMn[Fe(CN)_6]$ sample. Therefore, the NMFHFC samples showed superior cycling performance to that of the pristine $NaMn[Fe(CN)_6]$ sample. As a result, $Na_{1.60}Mn_{0.833}Fe_{0.167}[Fe(CN)_6]$ cathode material delivered an especially high energy density of 436 Wh kg^{-1}, and excellent cycle life, with 80.2% capacity retention over 300 cycles. Moreover, the synthetic method based on co-precipitation makes it feasible to produce the NMFHFC samples on the kilogram scale. Consequently, this work paves the way to the commercialization of sodium ion batteries.

4. Experimental Section

Synthesis of $Na_xFe_yMn_{1-y}[Fe(CN)_6]$ materials. Iron (Ⅱ) sulfate heptahydrate ($FeSO_4·7H_2O$), manganese acetate tetrahydrate ($Mn(CO_2CH_3)_2·4H_2O$), sodium ferrocyanide decahydrate ($Na_4Fe(CN)_6·10H_2O$), and sodium choloride (NaCl) were purchased from Sigma-Aldrich and used without any further purifying treatment. In a typical synthesis procedure for $Na_{1.08}Fe_{1/6}Mn_{5/6}[Fe(CN)_6]$ ($0 < x < 0.7$), 3 m mol $Na_4Fe(CN)_6$ $10H_2O$ and 12 g NaCl were dissolved into 60 mL deionized water, with the result denoted as solution A. 2.5 m mol $Mn(CO_2CH_3)_2$, 0.5 m mol $Fe(CO_2CH_3)_2$, and 12 g NaCl were dissolved into 60 mL deionized water, with the result denoted as solution B. Then, solution A was added dropwise into solution B under magnetic stirring. The suspension was aged for several hours before centrifuging. The resultant precipitate was washed with deionized water several times and then dried at 120 °C for 12 h. A series of $Na_xFe_yMn_{1-y}[Fe(CN)_6]$ (y = 0, 1/6, 1/3, 1/2, 2/3) samples were prepared by

the same procedure. $Na_xFe_{1/6}Mn_{5/6}[Fe(CN)_6]$, $Na_xFe_{1/3}Mn_{2/3}[Fe(CN)_6]$, $Na_xFe_{1/2}Mn_{1/2}[Fe(CN)_6]$, and $Na_xFe_{2/3}Mn_{1/3}[Fe(CN)_6]$ were denoted as NMFHFC-1, NMFHFC-2, NMFHFC-3, and NMFHFC-4, respectively. To compare with the $Na_yFe_xMn_{1-x}[Fe(CN)_6]$ samples, $NaMn[Fe(CN)_6]$ was prepared using the same method, with the sample denoted as NMHFC.

Structural characterization. The microstructure of the $Na_xFe_yMn_{1-y}[Fe(CN)_6]$ powders was characterized by X-ray powder diffraction (XRPD; GBC MMA diffractometer) with Cu Kα radiation at a scan rate of 2° min^{-1}. The morphology of the samples was investigated by field emission scanning electron microscopy (FESEM; JEOL JSM-7500FA) and scanning transmission electron microscopy (STEM) equipped with energy-dispersive X-ray spectroscopy (EDS). X-ray photoelectron spectroscopy (XPS) was conducted using a SPECS PHOIBOS 100 Analyser installed in a high-vacuum chamber with the base pressure below 10^{-8} mbar, and X-ray excitation was provided by Al Kα radiation with photon energy hv = 1486.6 eV at the high voltage of 12 kV and power of 120 W. Raman spectra were collected using a JOBIN Yvon Horiba Raman spectrometer model HR800, with a 10 mW helium/neon laser at 632.8 nm excitation in the range of 150 to 2000 cm^{-1}. The molar ratios of Na and Fe were measured by inductively coupled plasma (ICP) analysis (Elementar Vario EL CUBE). ^{57}Fe Mössbauer spectra of the samples were collected at 300 K by using a standard constant-acceleration spectrometer and a ^{57}CoRh source, and the spectrometer was calibrated at room temperature with α–ion foil. The magnetic measurements were carried out using a 14 T physical properties measurement system (PPMS), equipped with a vibrating sample magnetometer (VSM), over a wide temperature range from 5 K to 300 K in a 100 Oe magnetic field. The phases of NMFHFC-1, NMFHFC-2, NMFHFC-3, and NMFHFC-4 were identified by synchrotron powder X-ray diffraction at the powder diffraction beamline of the Australian Synchrotron (ANSTO), with wavelength of 0.7747 Å. In situ synchrotron XRPD data were collected with a Mythen-II detector on the powder diffraction beamline at the Australian

Synchrotron with a wavelength (λ) of 0.6888 Å, determined using the NIST LaB_6 660b standard reference material. Data were collected continuously in 30 s acquisitions during charge and discharge. The cell used for the data collection was charged at a current density of 20 mA g^{-1}, and the cut-off was 2 - 4 V.

Electrochemical characterization. Before making slurry, all the materials were heated at 150 °C for 24h in a vacuum oven. $Na_xFe_yMn_{1-y}[Fe(CN)_6]$ electrodes were prepared by mixing 80% active materials, 10% carbon black, and 10% polyvinylidene fluoride (PVDF) (used as binder) by weight to form an electrode slurry, which then was coated on aluminium foil, followed by drying in a vacuum oven overnight at 120 °C and then pressing at the pressure of 30 MPa. The active material loading rate was ~4 mg cm^{-2}. Sodium foil was cut by the doctor blade technique from sodium bulk stored in mineral oil, and it then was employed as both reference and counter electrode. A porous polypropylene film was used as the separator. The home-made electrolyte was 1.0 mol/L sodium perchlorate ($NaClO_4$ ACS reagent 98.0%, Sigma-Aldrich) in a 1 : 1 (v/v) mixture of ethylene carbonate (EC, anhydrous 99%, Sigma-Aldrich) and diethyl carbonate (DEC, anhydrous 99+%, Sigma-Aldrich). The chemicals were used without further drying. The cells were assembled in an argon-filled glove box. The electrochemical performances were tested on a Land Test System in the voltage range of 2 − 4.2 V (vs. Na^+/Na). Hard carbon electrodes were prepared by mixing 80% active materials, 10% carbon black, and 10% carboxylmethyl cellulose (CMC) (used as binder) by weight to form the electrode slurry, which then was coated on aluminium foil. NMFHFC-1/hard carbon full cells were assembled with NMFHFC-1 and hard carbon as cathode and anode electrodes, respectively.

*Computational methods***.** Density functional theory (DFT) calculations were performed using the VASP 5.4.4 code [1] on Australian Synchrotron Compute Infrastructure (ASCI). The generalized gradient approximation with the Hubbard potential (GGA+U) method was used with a Perdew-Burke-Ernzerhof (PBE) exchange correlation functional [2]. The interactions

between the ionic cores and the valence electrons were treated by ultrasoft pseudopotentials [3]. The *U* values for low spin Fe, high spin Fe, and Mn were set to 3.0, 7.0, and 5.0 eV, respectively. In all calculations, the cut-off energy of the plane wave was set at 600 eV, and a Monkhorst-Pack k-point grid was used to ensure that the total energy value convergence was within 1 meV/atom. The calculations of Na and Mn atoms substation in the structure were performed by constructing 2×2×2 supercells. To simplify the structure models, water content was not considered here in the calculations. During the lowest energy geometry optimization process, the tolerance convergence accuracy was set to the points when the total energy was less than 1.0×10^{-5} eV/atom, the maximum force on each atom was less than 0.01 eV/nm, the maximum stress was less than 0.01 GPa, and the maximum displacement between cycles was less than 1×10^{-4} eV.

Supporting Information ((delete if not applicable))
Supporting Information is available from the Wiley Online Library or from the author.

Acknowledgements

This work was supported by a Discovery Early Career Researcher Award (DECRA, No. DE180101478) of the Australian Research Council and an Australian Renewable Energy Agency (ARENA) Project (No. G00849). The authors would like to also thank Dr. Tania Silver for her critical reading of the manuscript, as well as Dr. Dongqi Shi for the XPS measurements. The authors also acknowledge the use of the facilities in the UOW Electron Microscopy Centre, with particular thanks to Dr. Gilberto Casillas-Garcia. Part of the experiments were conducted on the PD and XAS beamlines, Australian Synchrotron (ANSTO). DFT calculations were performed on ASCI.

Received: ((will be filled in by the editorial staff))
Revised: ((will be filled in by the editorial staff))
Published online: ((will be filled in by the editorial staff))

References

[1] D. Larcher, J. M. Tarascon, *Nat. Chem.* **2014**, *7*, 19.

[2] N. Yabuuchi, K. Kubota, M. Dahbi, S. Komaba, *Chem. Rev.* **2014**, *114*, 11636.

[3] X. Xiang, K. Zhang, J. Chen, *Adv.Mater.* **2015**, *27*, 5343.

[4] F. Xie, L. Zhang, D. Su, M. Jaroniec, S.-Z. Qiao, *Adv. Mater.* **2017**, *29*, 1700989.

[5] P. F. Wang, H. R. Yao, X. Y. Liu, J. N. Zhang, L. Gu, X. Q. Yu, Y. X. Yin, Y. G. Guo, *Adv. Mater.* **2017**, *29*, 1700210.

[6] W. J. Li, C. Han, W. Wang, F. Gebert, S.-L. Chou, H.-K. Liu, X. Zhang, S. X. Dou, *Adv. Energy Mater.* **2017**, *7*, 1700274.

[7] S. Guo, Q. Li, P. Liu, M. Chen, H. Zhou, *Nat. Commun.* **2017**, *8*, 135.

[8] C. Fang, Y. Huang, L. Yuan, Y. Liu, W. Chen, Y. Huang, K. Chen, J. Han, Q. Liu, Y. Huang, *Angew. Chem. Int. Ed.* **2017**, *56*, 6793.

[9] W. J. Li, C. Han, S. L. Chou, J. Z. Wang, Z. Li, Y. M. Kang, H. K. Liu, S. X. Dou, *Chem. Eur.J.* **2016**, *22*, 590.

[10] W. Li, C. Han, Q. Xia, K. Zhang, S. Chou, Y. M. Kang, J. Wang, H. K. Liu, S. X. Dou, *Small Methods* **2018**, *2*, 1700346.

[11] J. Deng, Q. Gong, H. Ye, K. Feng, J. Zhou, C. Zha, J. Wu, J. Chen, J. Zhong, Y. Li, *ACS Nano* **2018**, *12*, 1829.

[12] J. Kim, D. H. Seo, H. Kim, I. Park, J. K. Yoo, S. K. Jung, Y. U. Park, W. A. Goddard Iii, K. Kang, *Energy Environ. Sci.* **2015**, *8*, 540.

[13] E. Hosono, T. Saito, J. Hoshino, M. Okubo, Y. Saito, D. Nishio-Hamane, T. Kudo, H. Zhou, *J. Power Sources* **2012**, *217*, 43.

[14] S. Guo, H. Yu, D. Liu, W. Tian, X. Liu, N. Hanada, M. Ishida, H. Zhou, *Chem.Commun.* **2014**, *50*, 7998.

[15] S. Guo, H. Yu, P. Liu, Y. Ren, T. Zhang, M. Chen, M. Ishida, H. Zhou, *Energy Environ. Sci.* **2015**, *8*, 1237.

[16] Y. Li, Z. Yang, S. Xu, L. Mu, L. Gu, Y. S. Hu, H. Li, L. Chen, *Adv. Sci.* **2015**, *2*, 1500031.

[17] L. Mu, S. Xu, Y. Li, Y. S. Hu, H. Li, L. Chen, X. Huang, *Adv. Mater.* **2015**, *27*, 6928.

[18] Z. Jian, V. Raju, Z. Li, Z. Xing, Y. S. Hu, X. Ji, *Adv. Functn. Mater.* **2015**, *25*, 5778.

[19] Y. Fang, L. Xiao, X. Ai, Y. Cao, H. Yang, *Advance Materials* **2015**, *27*, 5895.

[20] Y. Qi, L. Mu, J. Zhao, Y. S. Hu, H. Liu, S. Dai, *Angew. Chem. Int. Ed.* **2015**, *54*, 9911.

[21] Y. Jiang, Z. Yang, W. Li, L. Zeng, F. Pan, M. Wang, X. Wei, G. Hu, L. Gu, Y. Yu, *Adv. Energy Mater.* **2015**, *5*, 1402104.

[22] Y. U. Park, D. H. Seo, H. Kim, J. Kim, S. Lee, B. Kim, K. Kang, *Adv.Funct.Mater.* **2014**, *24*, 4603.

[23] J. Ma, S. H. Bo, L. Wu, Y. Zhu, C. P. Grey, P. G. Khalifah, *Chem. Mater.* **2015**, *27*, 2387.

[24] D. Yuan, X. Liang, L. Wu, Y. Cao, X. Ai, J. Feng, H. Yang, *Adv. Mater.* **2014**, *26*, 6301.

[25] X. Wu, C. Wu, C. Wei, L. Hu, J. Qian, Y. Cao, X. Ai, J. Wang, H. Yang, *ACS Appl. Mater. Interfaces* **2016**, *8*, 5393.

[26] W. J. Li, S. L. Chou, J. Z. Wang, Y. M. Kang, J. L. Wang, Y. Liu, Q. F. Gu, H. K. Liu, S. X. Dou, *Chem. Mater.* **2015**, *27*, 1997.

[27] J. Song, L. Wang, Y. Lu, J. Liu, B. Guo, P. Xiao, J. J. Lee, X. Q. Yang, G. Henkelman, J. B. Goodenough, *J. Am. Chem. Soc.* **2015**, *137*, 2658.

[28] W. J. Li, S. L. Chou, J. Z. Wang, J. L. Wang, Q. F. Gu, H. K. Liu, S. X. Dou, *Nano Energy* **2015**, *13*, 200.

[29] Y. You, X. L. Wu, Y. X. Yin, Y. G. Guo, *Energy Environ. Sci.* **2014**, *7*, 1643.

[30] L. Wang, Y. Lu, J. Liu, M. Xu, J. Cheng, D. Zhang, J. B. Goodenough, *Angew. Chem. Int. Ed.* **2013**, *52*, 1964.

[31] A. Widmann, H. Kahlert, I. Petrovic-Prelevic, H. Wulff, J. V. Yakhmi, N. Bagkar, F. Scholz, *Inorg. Chem.* **2002**, *41*, 5706.

[32] C. Li, X. Han, F. Cheng, Y. Hu, C. Chen, J. Chen, *Nat. Commun.* **2015**, *6*, 7345.

[33] H. K. Schmid, W. Mader, *Micron* **2006**, *37*, 426.

[34] X. Jiang, T. Zhang, L. Yang, G. Li, J. Y. Lee, *ChemElectroChem* **2017**, *4*, 2237.

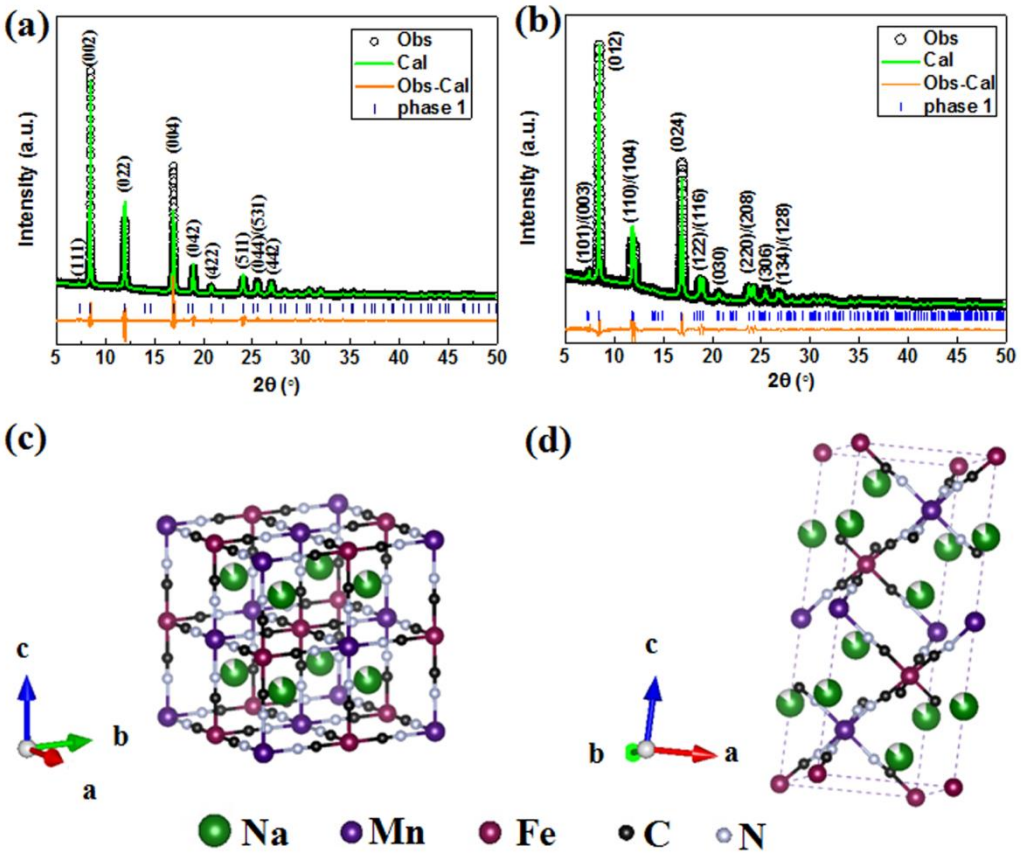

Figure 1. (a, b) Rietveld refinement of synchrotron X-ray powder diffraction (XRPD, λ =0.7747 Å) patterns and (c, d) crystal structures of (a, c) NMFHFC, and (b, d) NMHFC presented in a single unit cell. (R_B = 4.43%, R_{wp} = 7.52%, GoF = 1.872 in Figure 1(a); R_B = 3.31%, R_{wp} = 3.85%, GoF = 1.255 in Figure 1b)

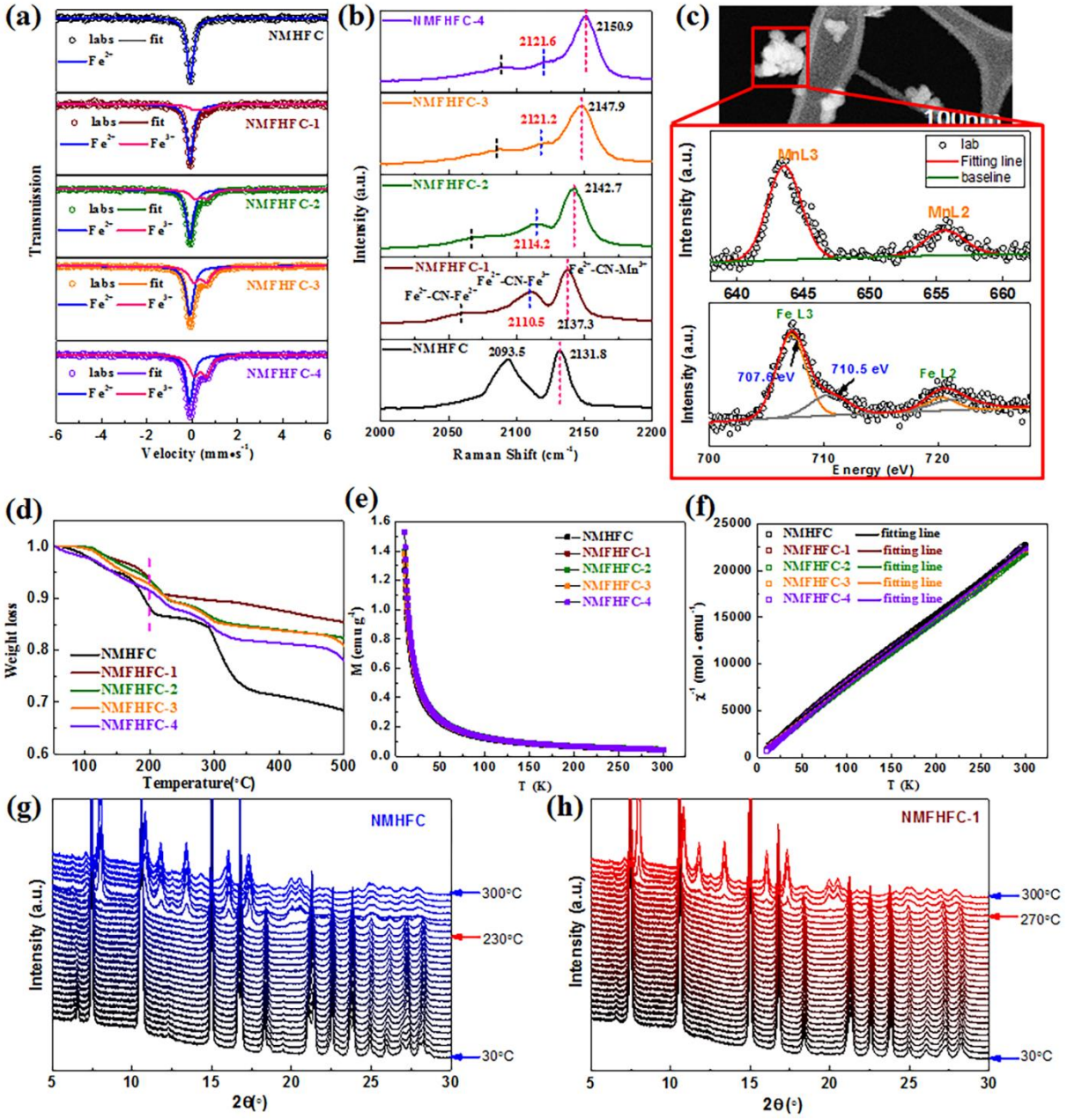

Figure 2. Characterization of NMFHFC samples compared with NMHFC: (a) Mössbauer spectra, (b) Raman spectra, (c) EELS spectra with the image of the selected particles at the top, (d) TGA curves, (e) temperature dependence of the magnetic susceptibility, and (f) inverse susceptibilities corrected for the temperature-independent contribution and their fit to the Curie-Weiss law. (g-h) Structural evolution of (g) NMHFC and (h) NMFHFC-1 during heating from 30° C to 300° C (The temperature interval is 10° C, and the data of NMHFC heated at 210°C is missed due to the beamline disturbance. λ=0.68684nm.).

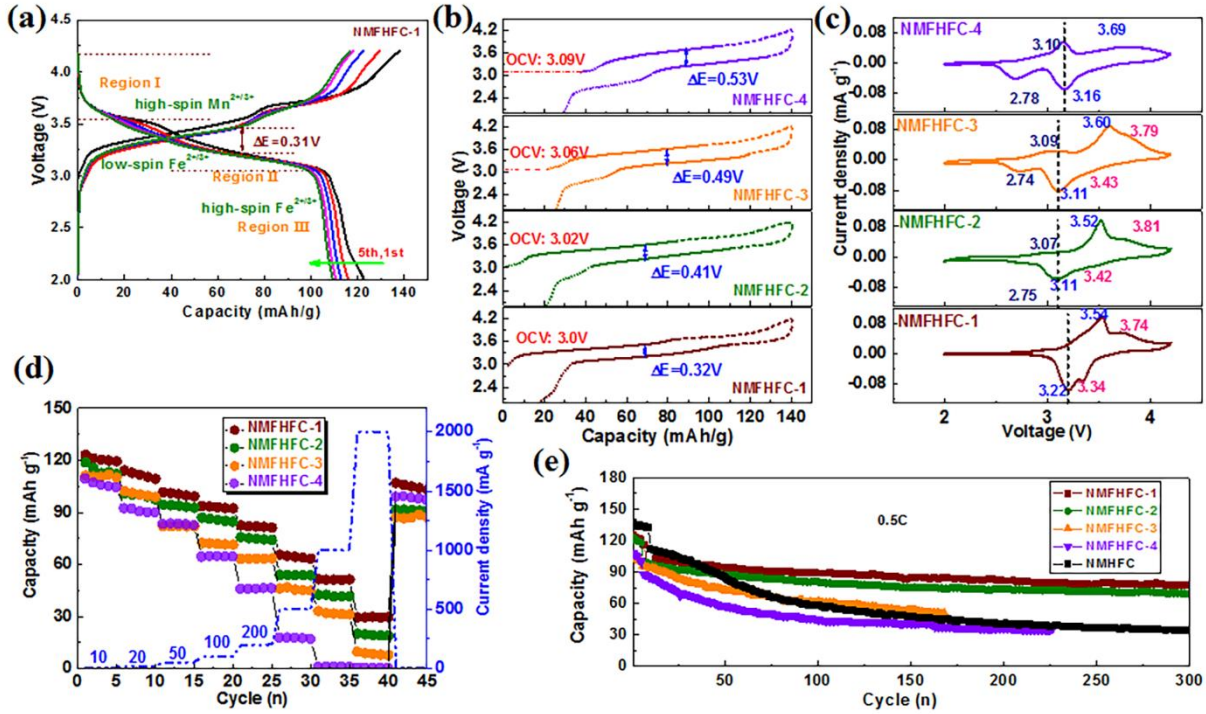

Figure 3. Electrochemical performance of NMFHFC composites: (a) Charge-discharge curves of NMFHFC-1 at the 0.1 C rate (1 C = 100 mA g^{-1}) in the first 5 cycles, (b) comparison of charge-discharge curves and (c) CV curves of NMFHFC samples in the first cycle, (d) rate capability, and (e) cycling performance of NMFHFC samples.

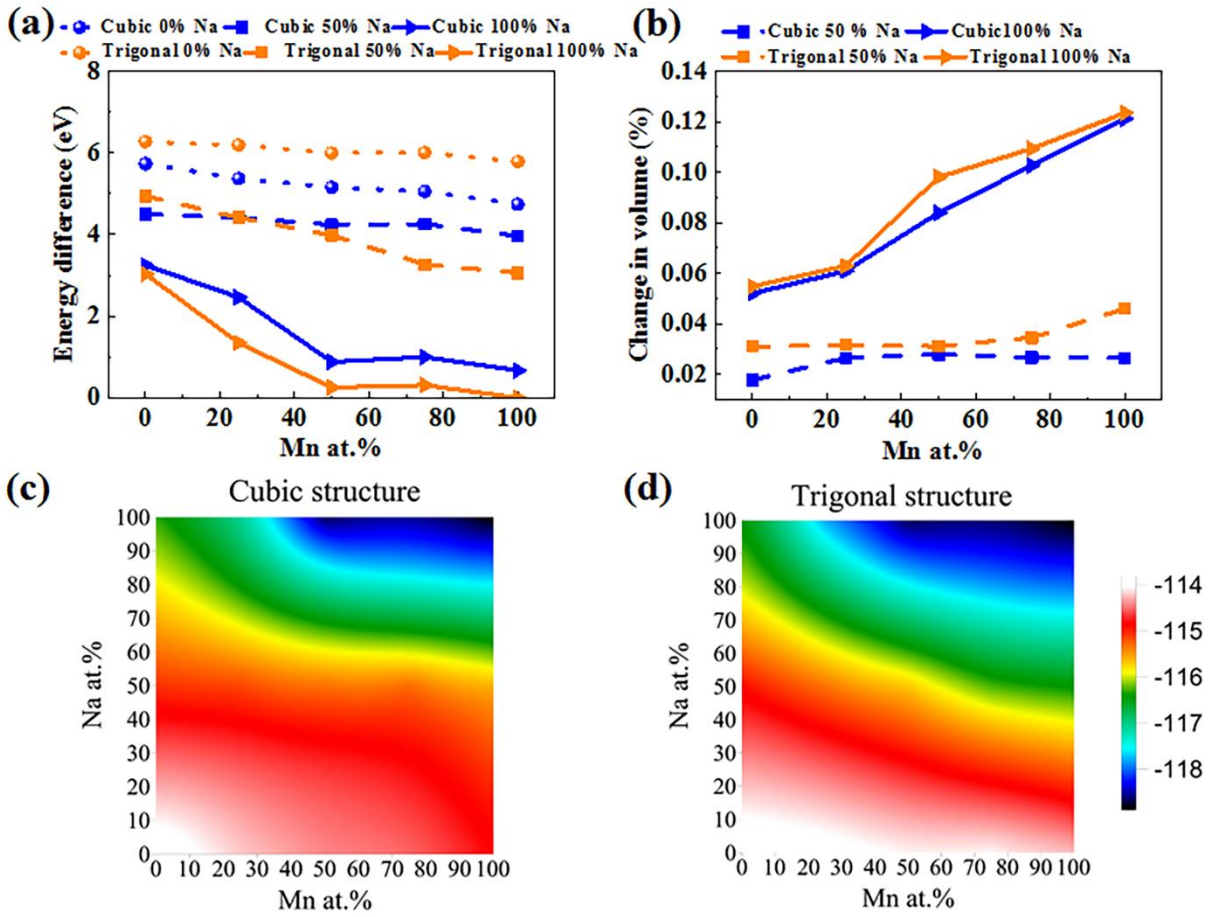

Figure 4. (a) Calculated difference in formation energy from variable Na and the Mn/Fe ratio in two different models of cubic and trigonal structures; (b) volume change of the selected structures. Note: the calculated cubic $Fe[Fe(CN)_6]$ structured unit cell is used as the reference volume; (c, d) 3D surface plot of total energy difference as a function of the Na ion occupancy percentage in the voids of the structure and the Mn atomic occupancy (Mn/Fe ratio) on the 3*b* sites in the framework in cubic (c) and trigonal (d) structures, respectively.

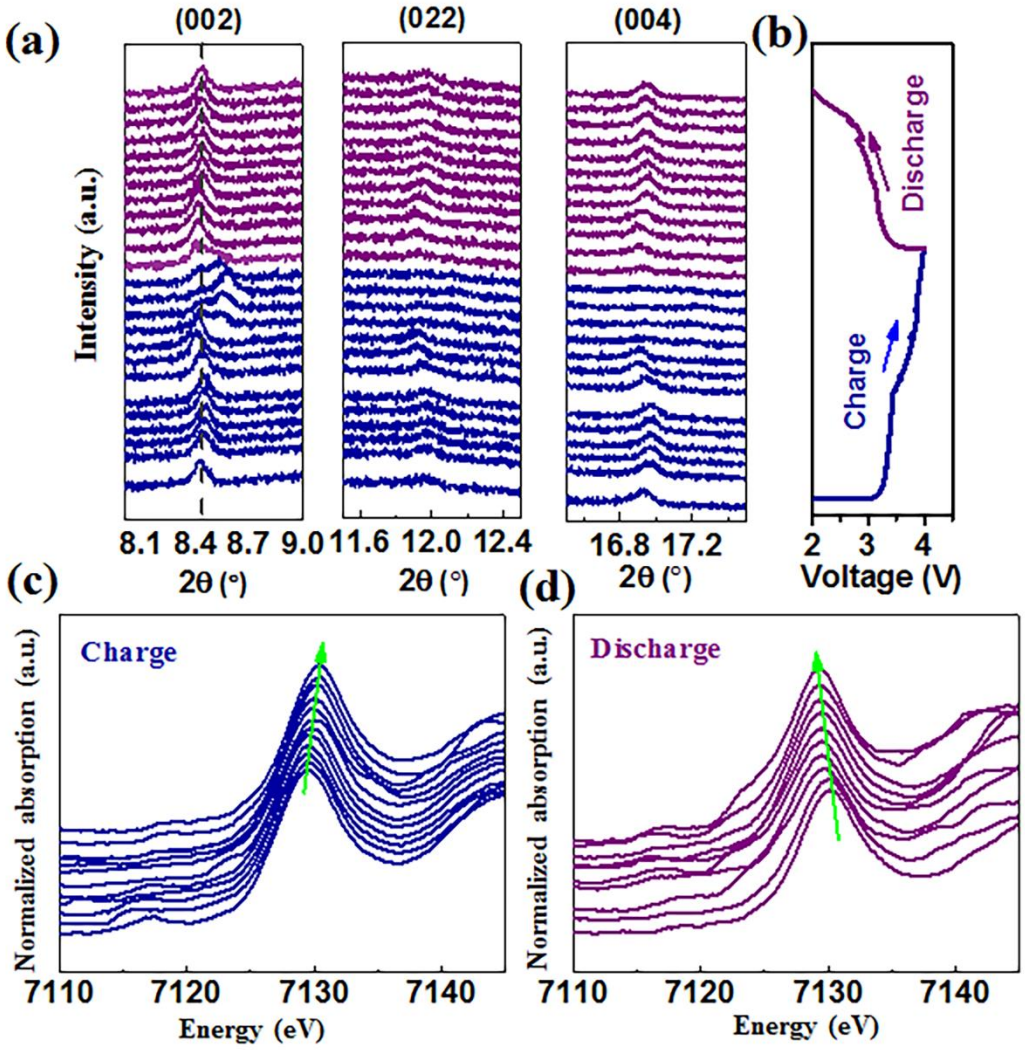

Figure 5. Evolution of NMFHFC-1 structure and the state of Fe in the [Fe(CN)6] group during the first charge and discharge at current density of 20 mA g^{-1}. (a) In-situ synchrotron PXRD patterns of NMFHFC-1 (where diffraction patterns of the (002), (022), and (004) reflections are stacked against the voltage profile (with the wavelength (λ) of 0.6888Å determined using the NIST LaB6 660b standard reference material.); (b) charge-discharge curves; and in-situ XANES spectra of the Fe K-edge for the NMHFC-1 sample during the (c) charge and (d) discharge process.

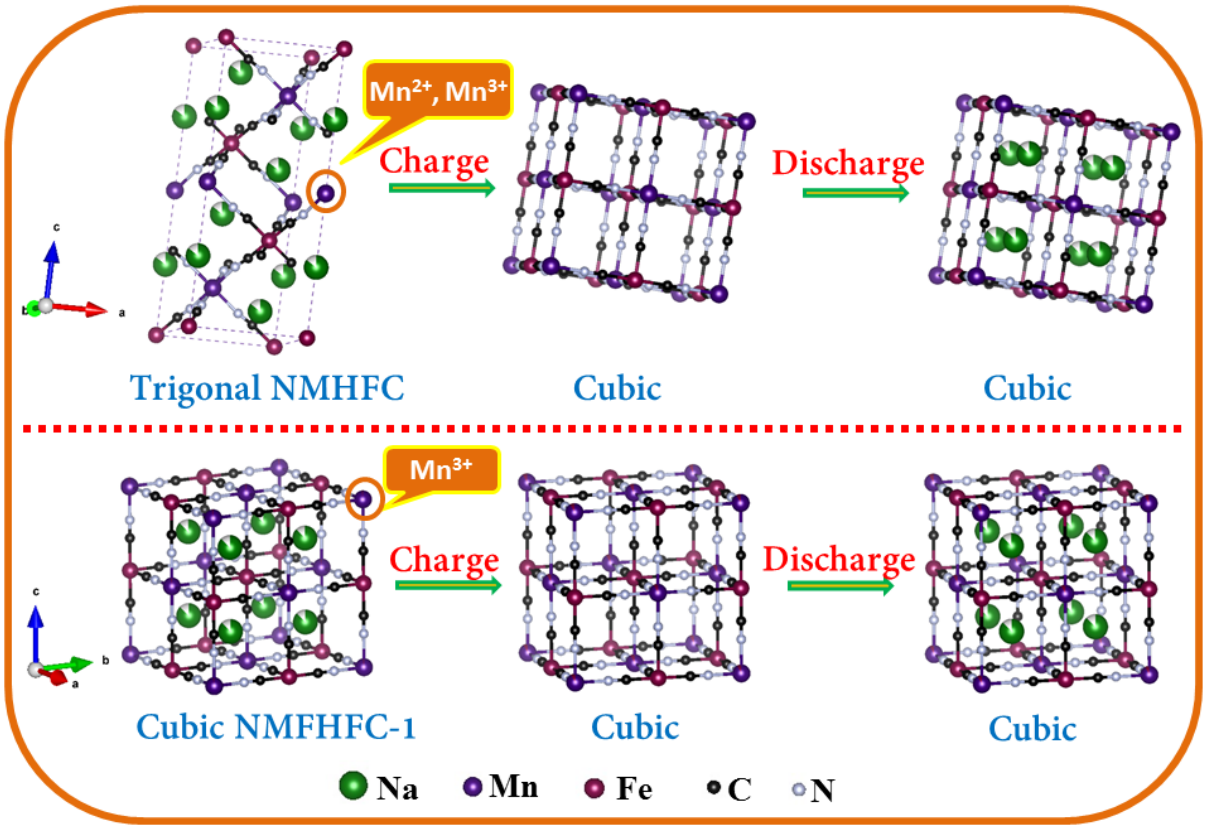

Figure 6. Structural evolution of NMHFC and NMFHFC-1 during the charge-discharge process.

A novel binary hexacyanoferrate (NMFHFC) with Na-rich and cubic structure was developed for the first time. Through multiple structural modulation, the stress distortion is minimized by restraining Mn^{2+} dissolution and the trigonal-cubic phase transition. Moreover, NMFHFC simultaneously retains rich Na ions in the framework. As a result, NMFHFC electrode delivered high energy density and excellent cycle life.

Keyword binary hexacyanoferrate, sodium-rich cubic phase, no phase transformation, Mn dissolution-free, minimized structural strain

Weijie Li,[a] Chao Han,[a] Wanlin Wang,[a] Qingbing Xia,[a] Shulei Chou,[a*] Qinfen Gu,[b*] Bernt Johannessen,[b] HuaKun Liu,[a] Shixue Dou[a]

Stress distortion restraint to boost the sodium ion storage performance of a novel binary hexacyanoferrate

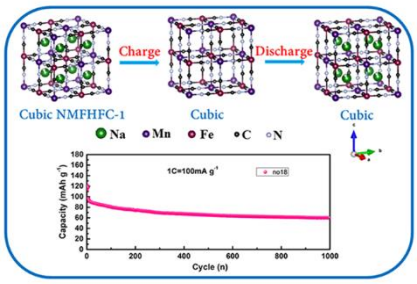

((Supporting Information can be included here using this template))

Supporting Information

Stress distortion restraint to boost the sodium ion storage performance of a novel binary hexacyanoferrate

Weijie Li,[a] Chao Han,[a] Wanlin Wang,[a] Qingbing Xia,[a] Shulei Chou,[a] Qinfen Gu,[b*] Bernt Johannessen,[b] HuaKun Liu,[a] Shixue Dou[a]*

Table of contents

1. Supporting results

Table S1. EDS results of the NMFHFC samples

Table S2. ICP results of the NMFHFC samples

Table S3. The crystal structure and lattice parameters of the NMFHFC samples refined by the Rietveld method.

Table S4. Crystallograpgic data of NFMHFC-1.

Table S5. Crystallographic data of NMFHFC-2.

Table S6. Crystallographic data of NMFHFC-2.

Table S7. Crystallographic data of NMFHFC-2.

Table S8. Crystallograpgic data of NMHFC.

Table S9 Valence state distribution of Fe in the NMFHFC samples based on analysis of the Mössbauer spectra.

Table S10 Peak positions of Raman spectra.

Table S11 Cycling stability Comparison of various Mn-based hexacyanoferrates reported

Table S12. SEM-EDS result for the NMFHFC-1 electrode after cycling for 100 cycles

Table S13. SEM-EDS results for NMFHFC-1 sample after storage in air for 2 years.

Figure S1. XRPD patterns of NMHFC and NMFHFC samples.

Figure S2. Synchrotron XRPD patterns of (a) NMFHFC-2, (b) NMFHFC-3, and (c) NMFHFC-4.

Figure S3. SEM images of the NMFHFC particles: (a) NMFHFC-1, (b) NMFHFC-2, (c) NMFHFC-3, and (d) NMFHFC-4.

Figure S4. The product yield of NMFHFC obtained from 130 mL solution and 50 L.

Figure S5. XPS results for (a) Fe $2p_{3/2}$ and (b) Mn $2p_{3/2}$ spectra.

Figure S6. The X-ray absorption near edge spectroscopy (XANES) patterns of NMFHFC-1 before and after cycling.

Figure S7. Initial charge-discharge curves of the NMFHFC-1 samples compared with NMHFC.

Figure S8. Charge-discharge curves of (a) NMHFC and (b) NMFHFC-1 after dehydrating at 180 ^{o}C for 24h at 0.5C rate.

Figure S9. Charge-discharge curves of the NMFHFC samples.

Figure S10. (a) Electrochemical impedance spectra (EIS) of NMFHFC samples, (b) The equivalent circuit used to interpret the EIS results.

Figure S11. Cyclic voltammetry (CV) curves of NMFHFC-1 at a variety of scanning rates: 0.1, 0.2, 0.3, 0.5, 0.8, 1.0, and 1.5 mV s^{-1} (a) and fitting from cyclic voltammetry experiments (square symbols) at the maximum of cathodic peak of NMFHFC-1(b).

Figure S12. Cyclic voltammetry (CV) curves of NMFHFC-1 at a variety of scanning rates: 0.1, 0.2, 0.3, 0.5, 0.8, 1.0, and 1.5 mV s^{-1} (a) and fitting from cyclic voltammetry experiments (square symbols) at the maximum of cathodic peak of NMFHFC-2(b).

Figure S13. Cyclic voltammetry (CV) curves of NMFHFC-1 at a variety of scanning rates: 0.1, 0.2, 0.3, 0.5, 0.8, 1.0, and 1.5 mV s^{-1} (a) and fitting from cyclic voltammetry experiments (square symbols) at the maximum of cathodic peak of NMFHFC-3(b).

Figure S14. Cyclic voltammetry (CV) curves of NMFHFC-1 at a variety of scanning rates: 0.1, 0.2, 0.3, 0.5, 0.8, 1.0, and 1.5 mV s^{-1} (a) and fitting from cyclic voltammetry experiments (square symbols) at the maximum of cathodic peak of NMFHFC-4(b).

Figure S15. Diffusion coefficients of NMFHFC samples calculated from CV curves.

Figure S16. Galvanostatic intermittent titration technique (GITT) plots for NMFHFC-1: (a) GITT discharging curve during cycling as a function of time in the voltage range of 3.2-4.2 V. (b) Plot of voltage vs. time ($\tau^{1/2}$) for the same titration to show the linear fit. (c) Voltage profiles before, during, and after a constant current pulse at 3.45 V, with schematic labelling of the different parameters. (d) The Na^+ diffusion coefficients (D_{Na^+}) calculated from the GITT curves for the NMFHFC electrodes as a function of cell voltage during the charge process.

Figure S17. Comparison of Na^+ diffusion coefficients of NMFHFC samples calculated from GITT.

Figure S18. The charge-discharge curves of NMFHFC-1 at the 0.5 C rate after 300 cycle.

Figure S19. The cycling performance of NMFHFC-1 at the 1 C rate.

Figure S20. (a) Photograph and (b)EDS spectrum of the separator in the cell with NMFHFC-1 after 100 cycles.

Figure S21. XRPD pattern of NMFHFC-1 stored under ambient atmosphere for 2 years.

Figure S22. (a) charge-discharge curves and (b) coulombic efficiency of hard carbon, (c) the charge/discharge curves and (d) the cycling performance of NFMHFC-1/hard carbon full cell at voltage range of 2.0-3.8V.

Figure S23. Electrochemical performance of B-NMFHFC-1: (a) charge-discharge curves, (b) cycling performance.

Table S1. EDS results of the NMFHFC samples

Sample	**Na (at%)**	**Mn (at%)**	**Fe (at%)**	**Na/(Mn+Fe)**
NMHFC	46.04	27.09	26.87	0.853
NMFHFC-1	44.48	23.14	32.38	0.801
NMFHFC-2	42.81	20.39	36.80	0.749
NMFHFC-3	41.89	16.12	41.99	0.721
NMFHFC-4	41.31	11.02	47.67	0.704

Table S2. ICP results of the NMFHFC samples

Sample	**Na (at%)**	**Mn (at%)**	**Fe (at%)**	**Na/(Fe+Mn)**
NMFHFC-1	44.53	23.13	32.34	0.803
NMFHFC-2	42.93	20.37	36.70	0.752
NMFHFC-3	42.06	16.01	41.93	0.726
NMFHFC-4	41.42	11.03	47.55	0.707

According to ICP results, the formula of NMFHFC samples was obtained, $Na_{1.60}Mn_{0.833}Fe_{0.167}[Fe(CN)_6]$, $Na_{1.40}Mn_{0.667}Fe_{0.333}[Fe(CN)_6]_{0.87}$, $Na_{1.31}Mn_{0.5}Fe_{0.5}[Fe(CN)_6]_{0.81}$, $Na_{1.25}Mn_{0.333}Fe_{0.667}[Fe(CN)_6]_{0.77}$ for NMFHFC-1, NMFHFC-2, NMFHFC-3, and NMFHFC-4, respectively, indicating that the amount of vacancies increased with more Fe being introduced into framework.

Table S3. The crystal structure and lattice parameters of the NMFHFC samples refined by XRPD patterns.

Sample	Phase	Lattice parameters (Å)
NMHFC	Trigonal, R-3(148)	a=7.539, c=17.919
NMFHFC-1	cubic, Fm-3m	a=10.515
NMFHFC-2	cubic, Fm-3m	a=10.486
NMFHFC-3	cubic, Fm-3m	a1=10.508
	cubic, Fm-3m	a2=10.369
NMFHFC-4	cubic, Fm-3m	a1=10.474
	cubic, Fm-3m	a2=10.305

Table S4. Crystallographic data of NFMHFC-1.

Atom	x	y	z	Occ.	B
N	0.8004	0.0000	0.0000	1	0.5
C	0.3071	0.0000	0.0000	1	0.5
Na	0.2500	0.2500	0.2500	0.8839	3.4
Fe1	0.5000	0.5000	0.5000	1	1.04
Mn	0.0000	0.0000	0.0000	0.977	1.46
Fe2	0.0000	0.0000	0.0000	0.023	1.46

Table S5. Crystallographic data of NMFHFC-2.

Atom	x	y	z	Occ.	B
N	0.1981	0.0000	0.0000	1	1.51
C	0.2874	0.0000	0.0000	1	1.51
Na	0.2500	0.2500	0.2500	0.851	3.11
Fe	0.5000	0.5000	0.5000	1	1.7
Mn/Fe	0.0000	0.0000	0.0000	1	1.5

Table S6. Crystallographic data of NMFHFC-3.

Atom	x	y	z	Occ.	B
Phase 1					
N	0.1967	0.0000	0.0000	1	1.51
C	0.2800	0.0000	0.0000	1	1.51
Na	0.2500	0.2500	0.2500	0.938	3.1
Fe	0.5000	0.5000	0.5000	1	1.6
Mn/Fe	0.0000	0.0000	0.0000	1	1.9
Phase 2					
N	0.1948	0.0000	0.0000	1	1.51
C	0.2839	0.0000	0.0000	1	1.51
Na	0.2500	0.2500	0.2500	0.863	3.2
Fe	0.5000	0.5000	0.5000	1	1.5
Mn/Fe	0.0000	0.0000	0.0000	1	1.6

Table S7. Crystallographic data of NMFHFC-4.

Atom	x	y	z	Occ.	B
Phase 1					
N	0.2012	0.0000	0.0000	1	1.53
C	0.2740	0.0000	0.0000	1	1.53
Na	0.2500	0.2500	0.2500	1.11	3.2
Fe	0.5000	0.5000	0.5000	1	1.1
Mn/Fe	0.0000	0.0000	0.0000	1	1.4
Phase 2					
N	0.2012	0.0000	0.0000	1	1.53
C	0.2740	0.0000	0.0000	1	1.53
Na	0.2500	0.2500	0.2500	1.11	3.2
Fe	0.5000	0.5000	0.5000	1	1.1
Mn/Fe	0.0000	0.0000	0.0000	1	1.4

Table S8. Crystallograpgic data of NMHFC.

Atom	x	y	z	Occ.	B
N1	0.2728	0.1261	0.4266	1	1
C1	0.4255	0.2066	0.3958	1	1
Na1	0.6667	0.3333	0.5777	0.86	1
Fe1	0.0000	0.0000	0.0000	1	1
Mn1	0.3333	0.6667	0.1667	0.977	1

Table S9 Valence state distribution of Fe in the NMFHFC samples based on analysis of the Mössbauer spectra.

Sample	**Fe^{2+} (%)**	**Fe^{3+} (%)**
NMFHFC-1	76.1(71)	23.9(94)
NMFHFC-2	66.7(25)	33.3(32)
NMFHFC-3	55.8(24)	44.2(31)
NMFHFC-4	49.5(22)	50.5(28)
NMHFC	100	

Table S10 Peak positions of Raman spectra.

Sample	**Fe^{2+}-CN-Fe^{2+}**	**Fe^{2+}-CN-Fe^{3+}**	**Fe^{2+}-CN-Mn^{3+}**
NMFHFC-1	2061.6 cm^{-1}	2110.5 cm^{-1}	2137.3 cm^{-1}
NMFHFC-2	2079.4 cm^{-1}	2114.2 cm^{-1}	2142.7 cm^{-1}
NMFHFC-3	2087.9 cm^{-1}	2121.2 cm^{-1}	2147.9 cm^{-1}
NMFHFC-4	2092.3 cm^{-1}	2121.6 cm^{-1}	2150.9 cm^{-1}
sample		Fe^{2+}-CN-Mn^{2+}	Fe^{2+}-CN-Mn^{3+}
NMHFC	2093.5 cm^{-1}	2131.8 cm^{-1}	

Table S11 Cycling stability Comparison of various Mn-based hexacyanoferrates reported

Materials	Cycles	Capacity retention (%)	Capacity degradation (mAh/g/cycle)
Trigonal $Na_{1.72}Mn[Fe(CN)_6]$[1]	30	90.3	0.433
Cubic $Na_{1.40}Mn[Fe(CN)_6]$[1]	30	96.0	0.164
Trigonal $Na_{1.72}Mn[Fe(CN)_6]$@Ppy[2]	200	67.0	0.312
Dehydrated trigonal $Na_{1.72}Mn[Fe(CN)_6]$[3]	500	70.0	0.086
Cubic $Na_{1.60}Mn_{0.833}Fe_{0.167}[Fe(CN)_6]$ in this work	300	80.2	0.083

Table S12. SEM-EDS result for the NMFHFC-1 electrode after cycling for 100 cycles compared with NMHFC

NMFHFC-1	**Na (at%)**	**Mn (at%)**	**Fe (at%)**	**Na/(Mn+Fe)**
Point 1	45.09	23.04	31.87	
Point 2	45.03	22.98	31.99	
Point 3	44.92	22.92	32.16	
Point 4	43.25	23.16	33.59	
average	44.57	23.03	32.40	0.804
NMHFC	**Na (at%)**	**Mn (at%)**	**Fe (at%)**	**Na/(Mn+Fe)**
Point 1	43.99	26.12	29.89	
Point 2	44.02	25.89	30.09	
Point 3	44.16	25.91	29.93	
average	44.06	25.97	29.97	0.788

Table S13. SEM-EDS results for NMFHFC-1 sample after storage in air for 2 years

	Na（at%）	**Mn (at%)**	**Fe (at%)**	**Na/(Mn+Fe)**
No. 1	44.87	22.12	33.01	
No. 2	45.55	21.54	32.91	
No. 3	42.20	24.74	33.06	
No. 4	47.00	22.93	30.07	
No. 5	43.48	22.88	33.64	
average	44.62	22.84	32.54	0.806

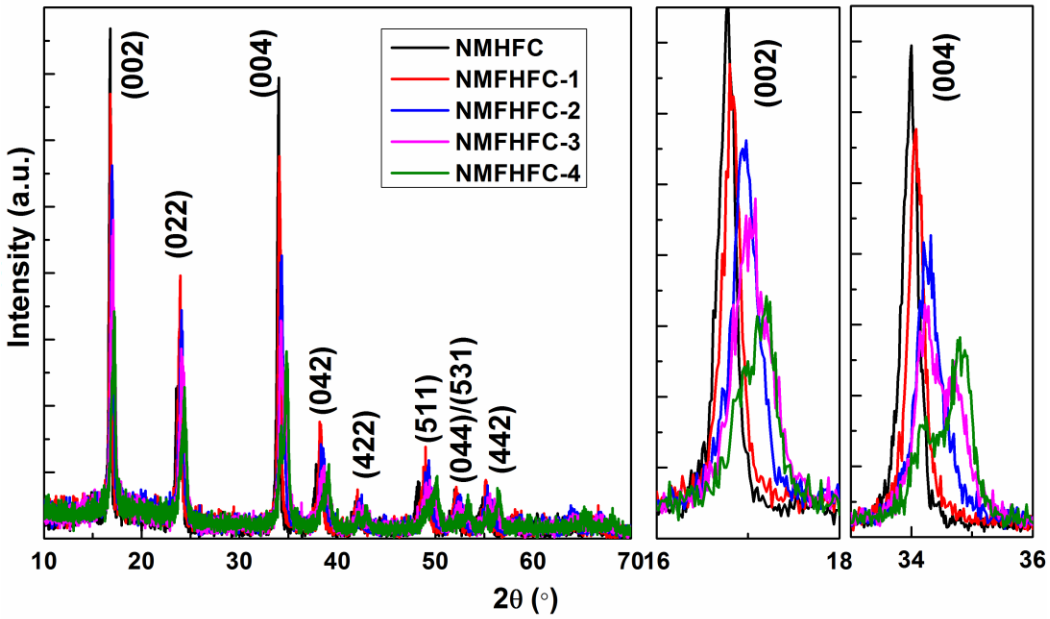

Figure S1. XRPD patterns of NMHFC and NMFHFC samples.

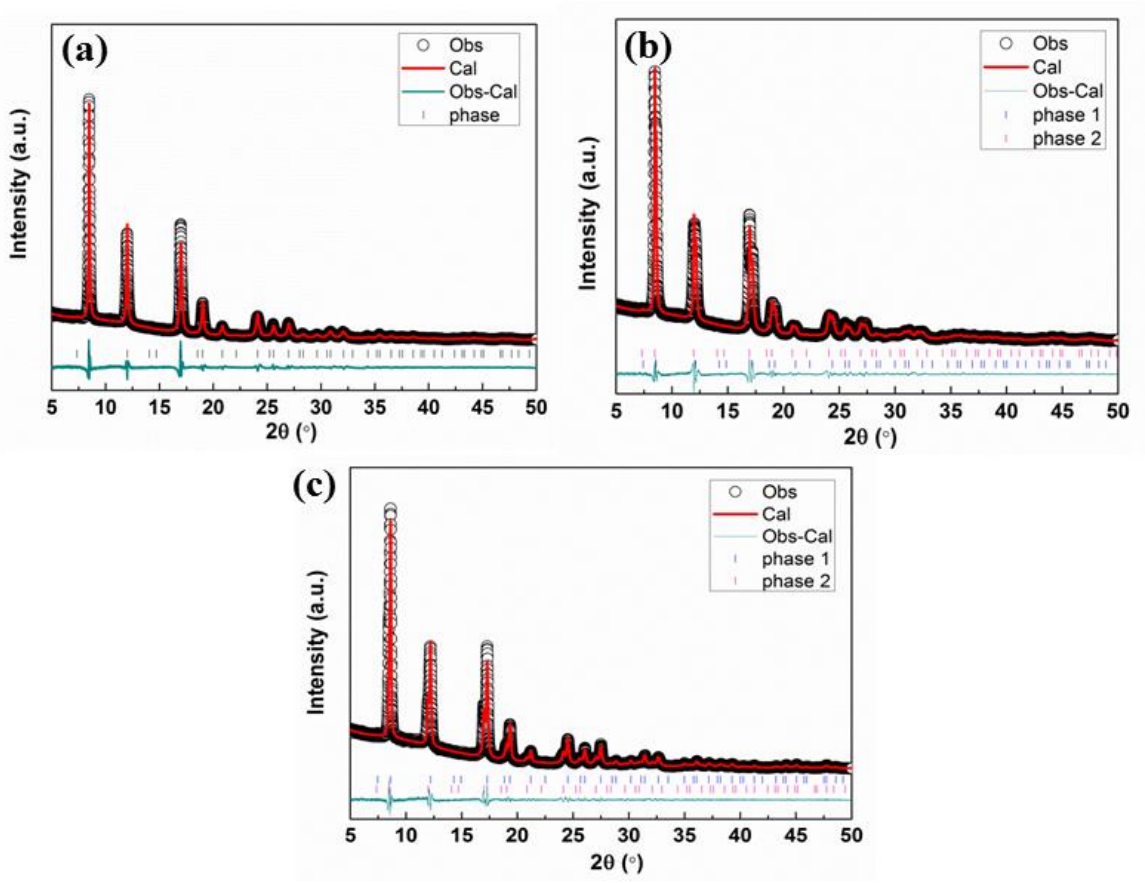

Figure S2. Rietveld refinement of synchrotron XRPD patterns of (a) NMFHFC-2, (b) NMFHFC-3, and (c) NMFHFC-4.

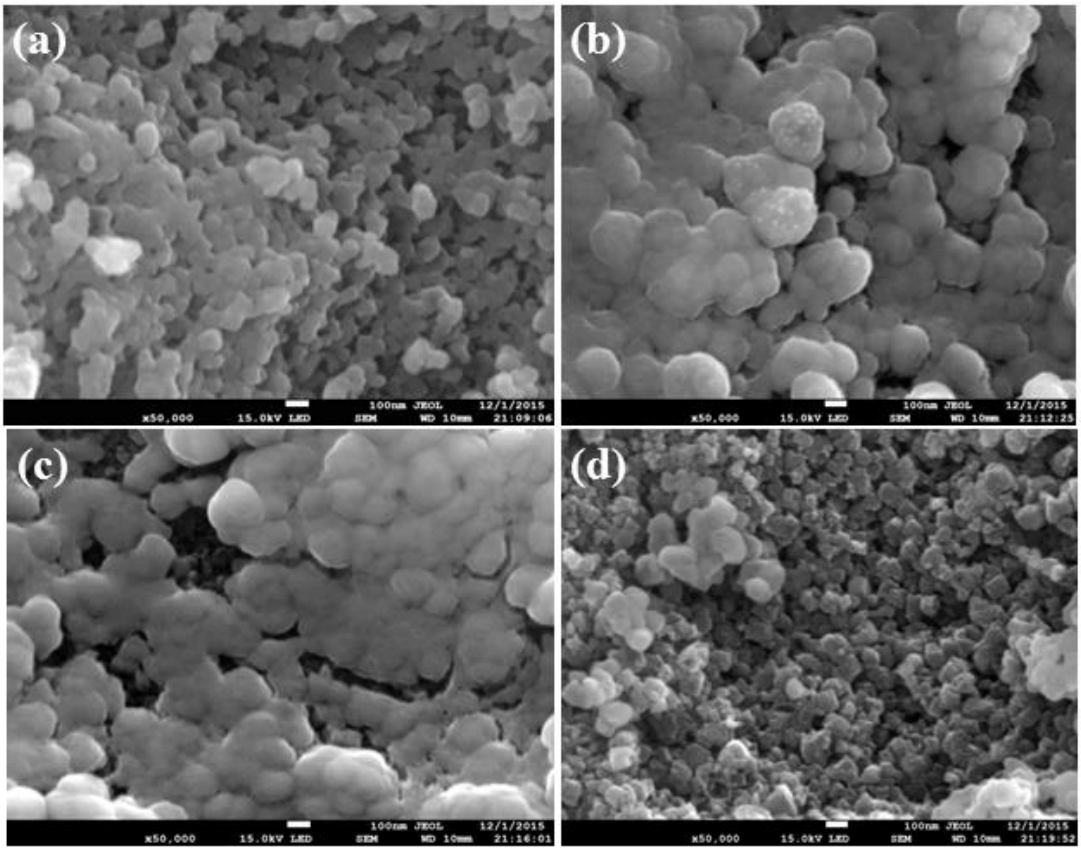

Figure S3. SEM images of the NMFHFC particles: (a) NMFHFC-1, (b) NMFHFC-2, (c) NMFHFC-3, (d) NMFHFC-4.

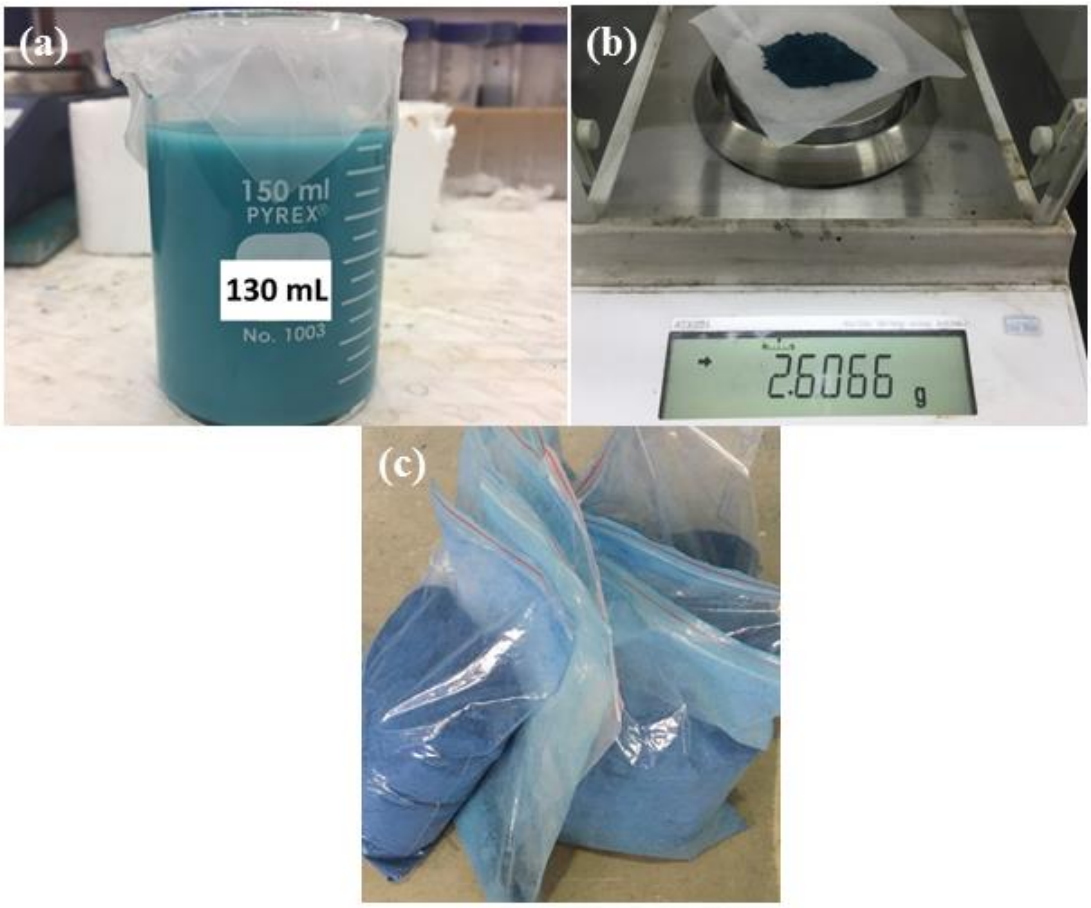

Figure S4. The product yield of NMFHFC obtained from (a,b)130 mL solution and (c)50 L.

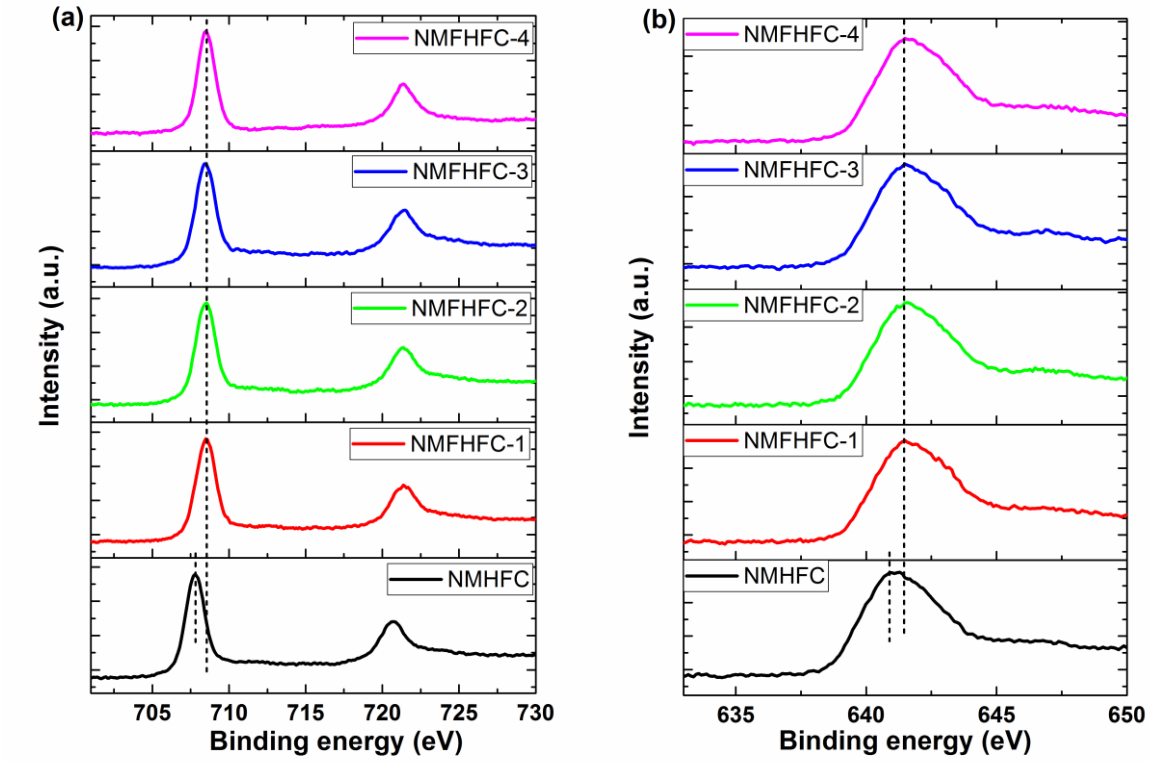

Figure S5. XPS results for (a) Fe $2p_{3/2}$ and (b) Mn $2p_{3/2}$ spectra.

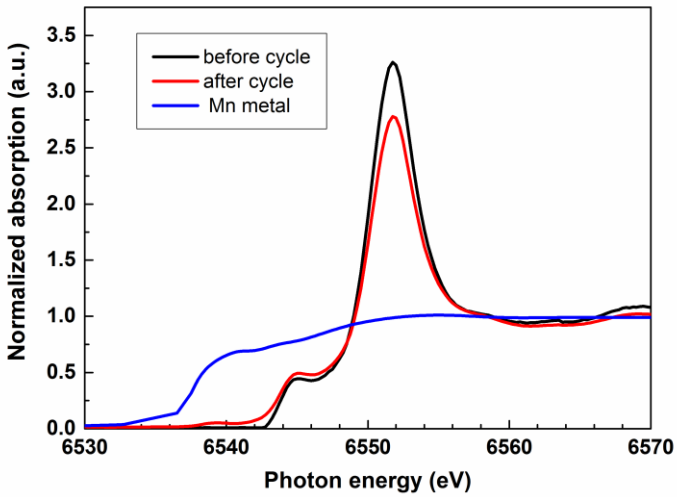

Figure S6. The X-ray absorption near edge spectroscopy (XANES) patterns of NMFHFC-1 before and after cycling.

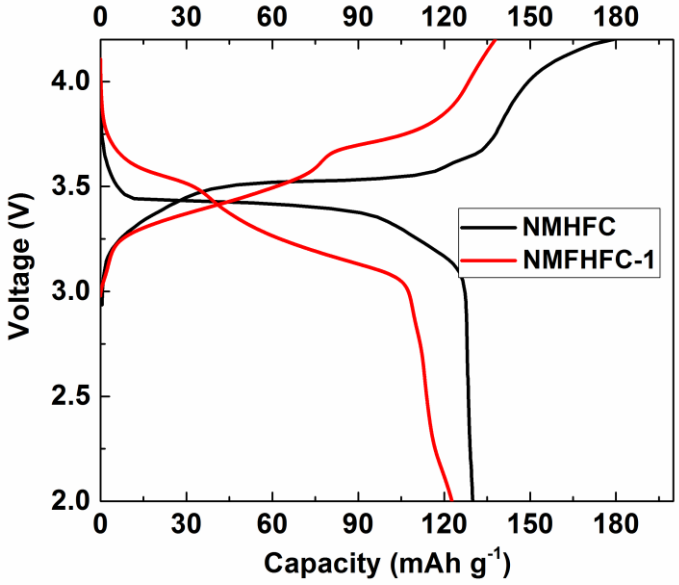

Figure S7. Initial charge-discharge curves of the NMFHFC-1 samples compared with NMHFC which are heated at 150 °C for 24h before electrochemical evolution.

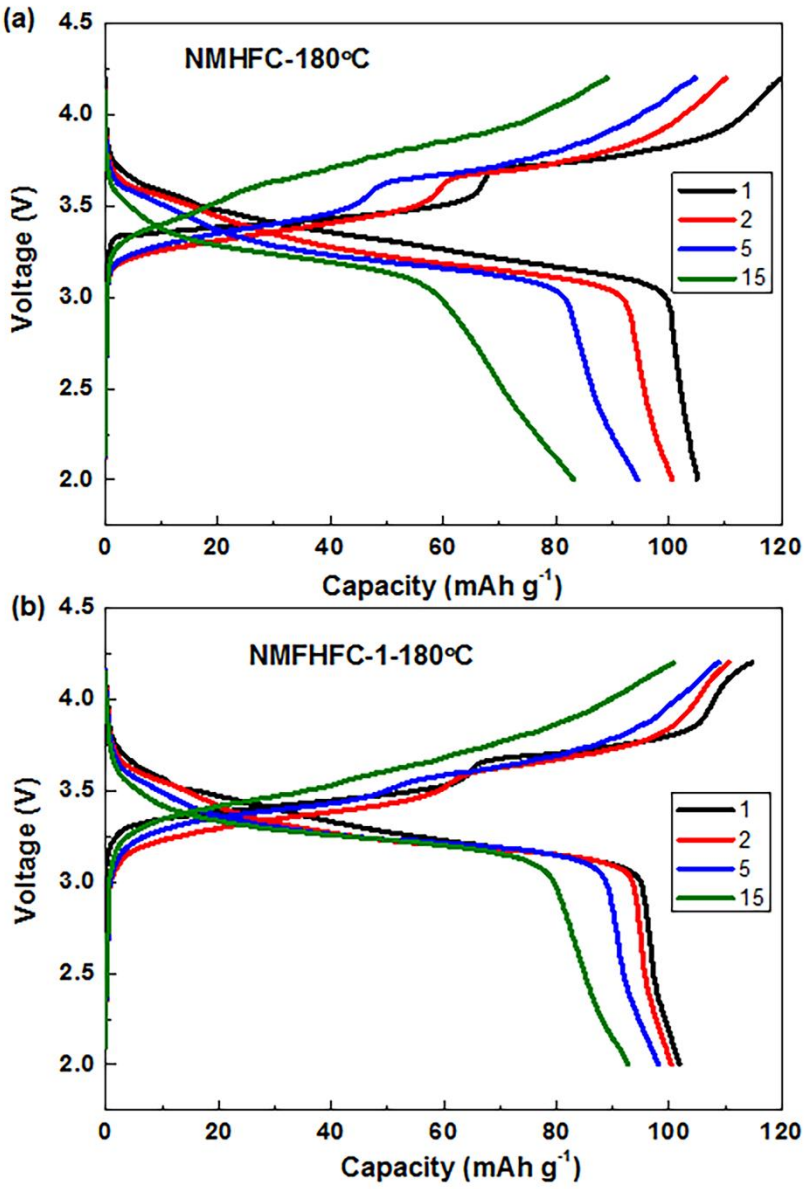

Figure S8. Charge-discharge curves of (a) NMHFC and (b) NMFHFC-1 after dehydrating at 180 °C for 24h at 0.5C rate.

In order to avoid moisture disturbance, NMHFC and NMFHFC-1 samples undergo dehydration at 180 ºC for 24h before preparing electrodes. According to TGA and in-situ high temperature synchrotron XRPD, NMHFC and MMFHFC-1 heated at 180 ºC have been removed the zeolitic water but the structure was not been damaged. NMFHFC-1-180 still presents the more stable cycling performance than that of NMHFC, demonstrating that the cycling stability of NMFHFC-1 comes from the stress distortion restrain by restraining Mn^{2+} dissolution and the trigonal-cubic phase transition.

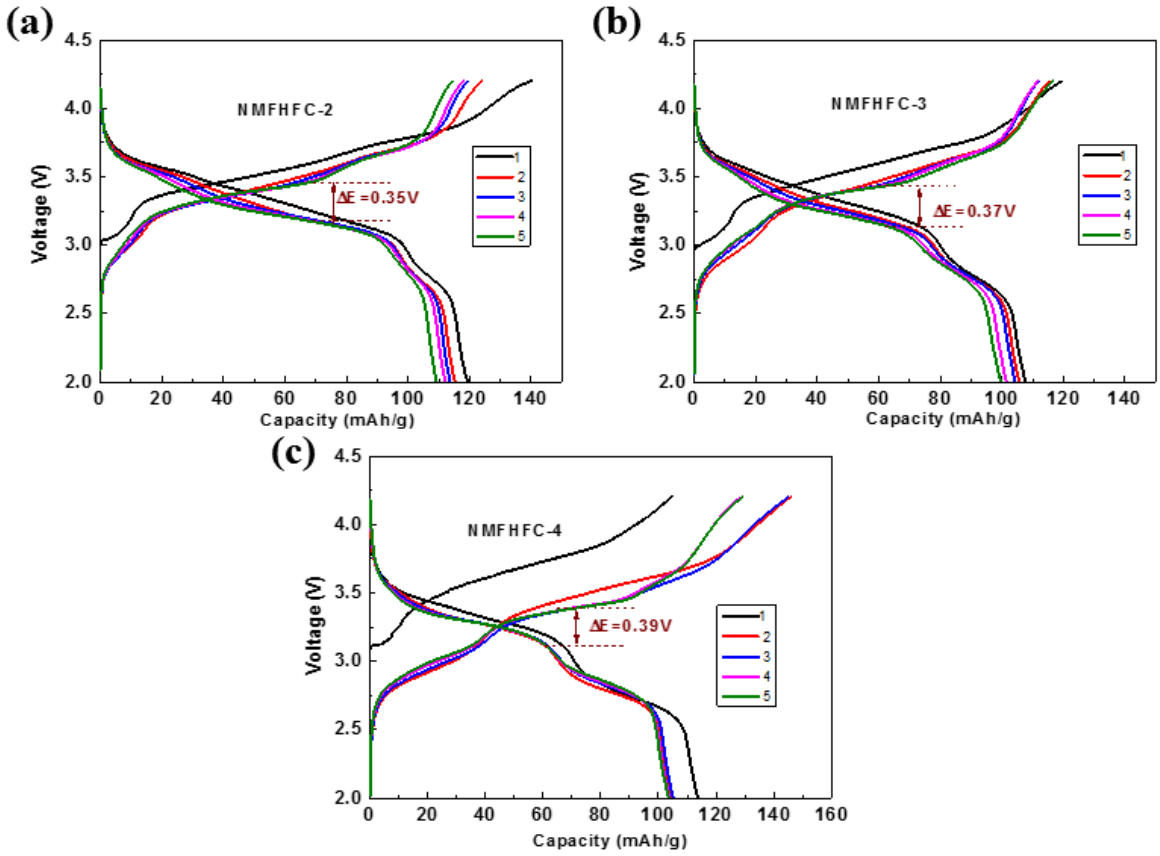

Figure S9. Charge-discharge curves of the NMFHFC samples: (a) NMFHFC-2, (b) NMFHFC-3, (c) NMFHFC-4.

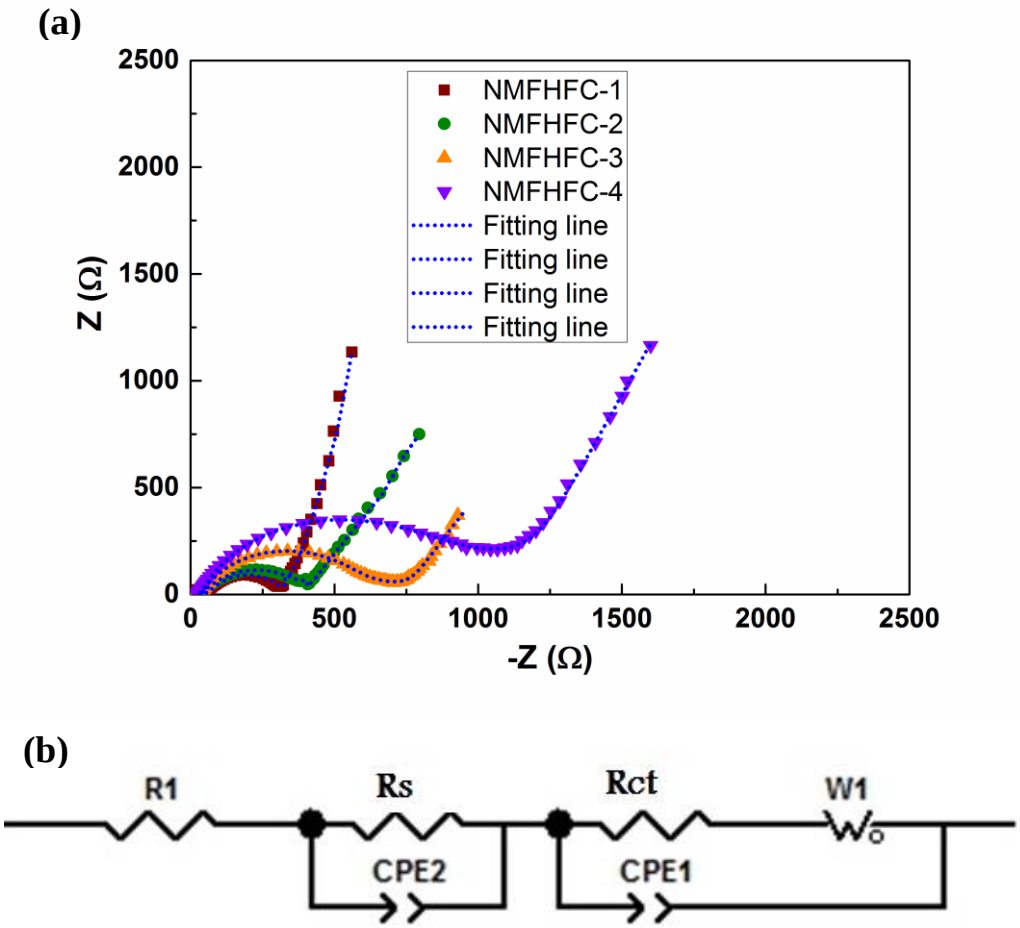

Figure S10. (a) Electrochemical impedance spectra (EIS) of NMFHFC samples, (b) The equivalent circuit used to interpret the EIS results.

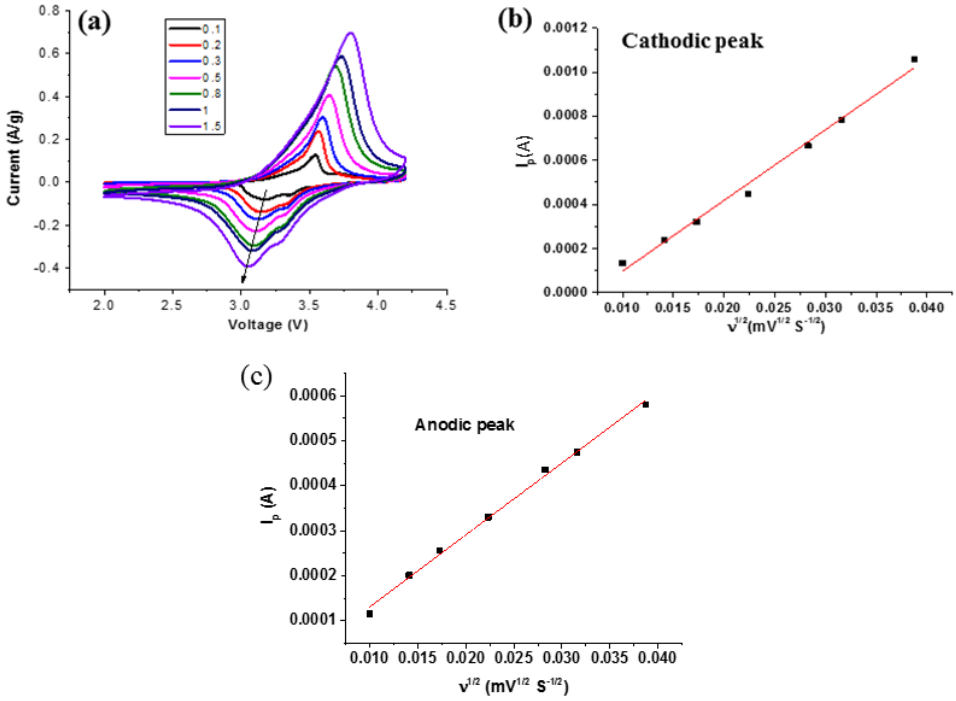

Figure S11. Cyclic voltammetry (CV) curves of NMFHFC-1 at a variety of scanning rates: 0.1, 0.2, 0.3, 0.5, 0.8, 1.0, and 1.5 mV s^{-1} (a) and fitting from cyclic voltammetry experiments (square symbols) at the maximum of (b) cathodic peak and (c) anodic peak of NMFHFC-1.

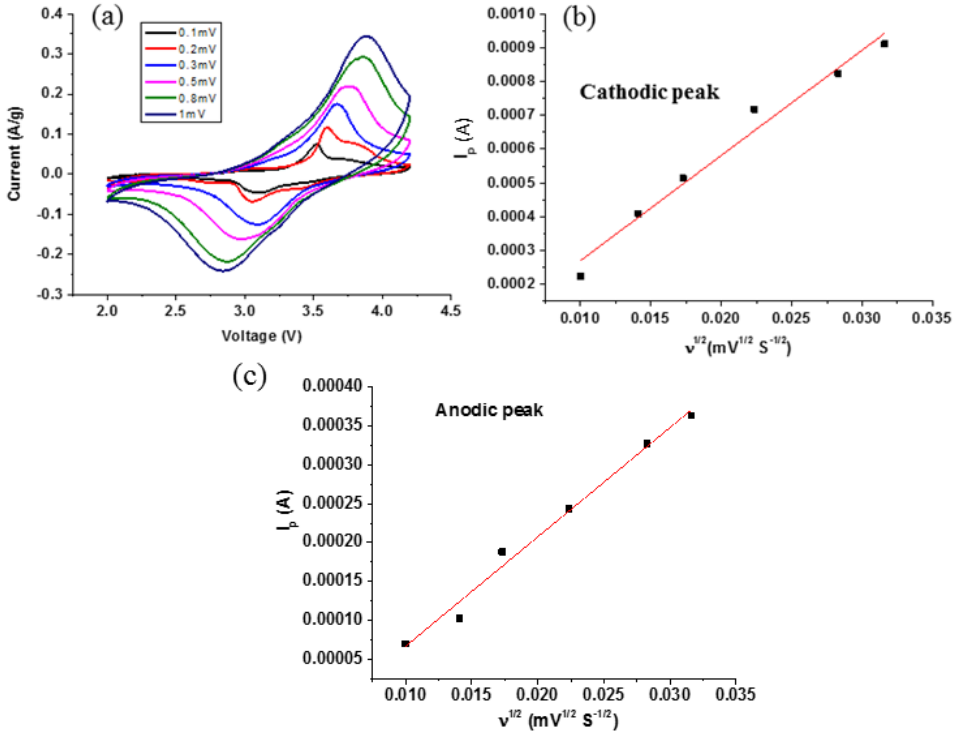

Figure S12. Cyclic voltammetry (CV) curves of NMFHFC-2 at a variety of scanning rates: 0.1, 0.2, 0.3, 0.5, 0.8, 1.0 and 1.5 mV s^{-1}(a) and fitting from cyclic voltammetry experiments (square symbols) at the maximum of (b) cathodic peak and (c) anodic peak of NMFHFC-2.

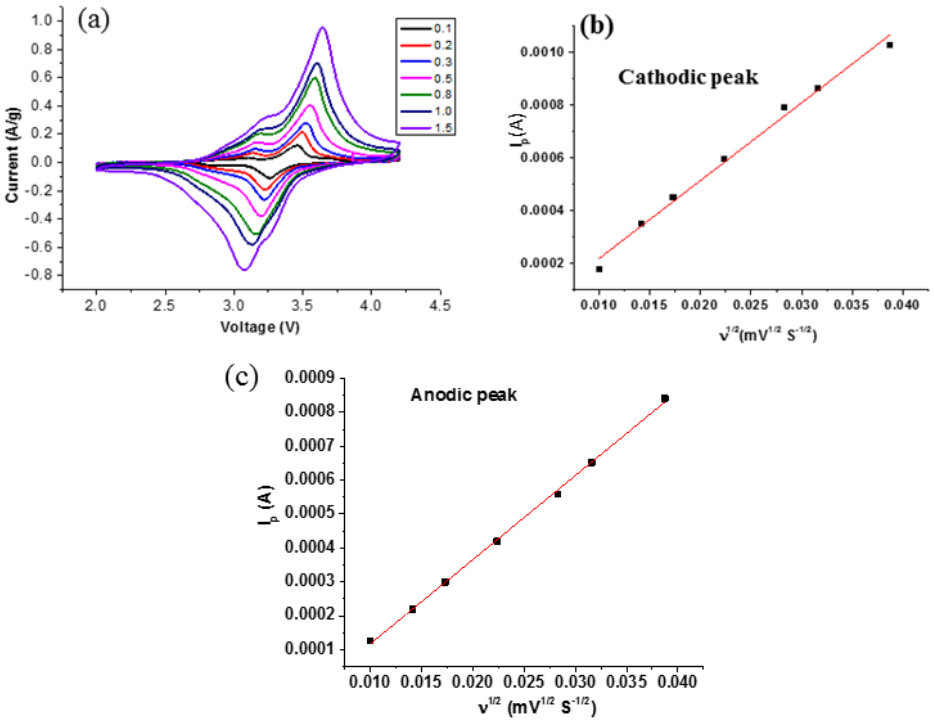

Figure S13. Cyclic voltammetry (CV) curves of NMFHFC-3 at a variety of scanning rates 0.1, 0.2, 0.3, 0.5, 0.8, 1.0 and 1.5 mV s^{-1}(a) and fitting from cyclic voltammetry experiments (square symbols) at the maximum of (b) cathodic peak and (c) anodic peak of NMFHFC-3.

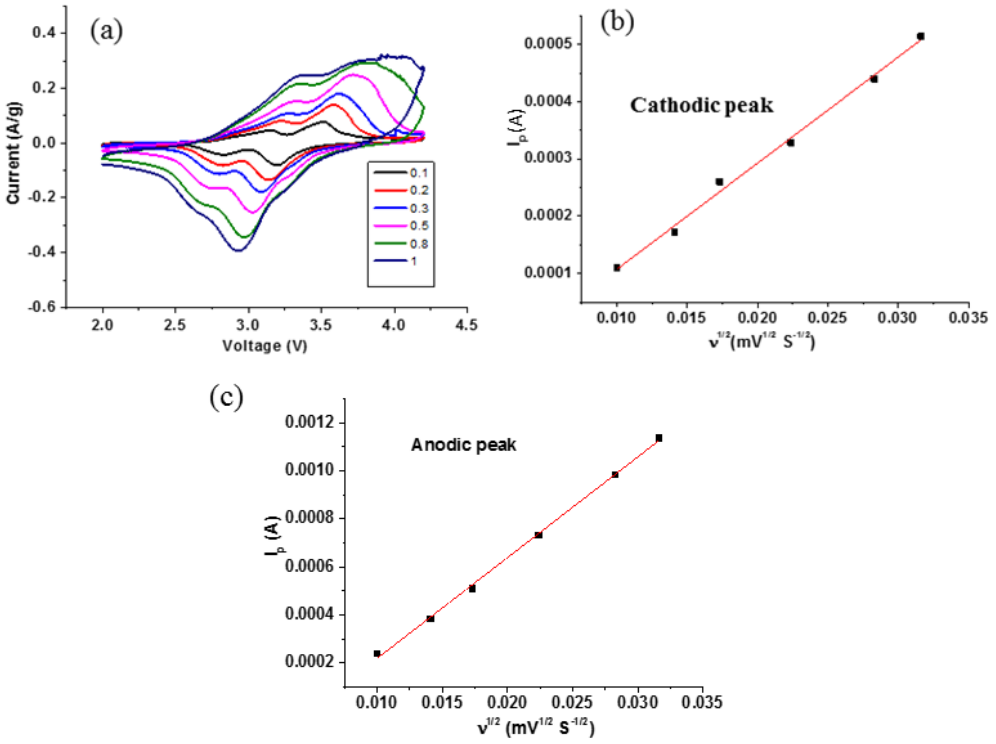

Figure S14. Cyclic voltammetry (CV) curves of NMFHFC-4 at a variety of scanning rates: 0.1, 0.2, 0.3, 0.5, 0.8, 1.0 and 1.5 mV s^{-1} (a) and fitting from cyclic voltammetry experiments (square symbols) at the maximum of (b) cathodic peak and (c) anodic peak of NMFHFC-4.

Figures S11-S14 show the cyclic voltammetry (CV) curves of the NMFHFC samples at a variety of scanning rates: 0.1, 0.2, 0.3, 0.5, 0.8, 1.0 and 1.5 mV s^{-1}.

The Na diffusion coefficient (*D*) can be evaluated by the Randles-Sevcik equation: [4]

$$I_p = 2.69 \times 10^5 \, n^{3/2} A D^{1/2} v^{1/2} C_0 \quad (1),$$

Where I_p is the peak current (A), *n* is the charge-transfer number, *A* is the geometric area of electrode (cm^3), C_0 is the concentration of Na^+ in the solution, *v* is the potential scan rate (V/s), and D is the diffusion coefficient of Na^+. Thus, the diffusion coefficient *D* can be calculated according to the peak currents at different potential scan rate. Then, the diffusion coefficients *D* of the NMFHFC samples are plotted in Figure S15. It is notable that the *D* of NMFHFC-1 is larger than those of the other NMFHFC samples.

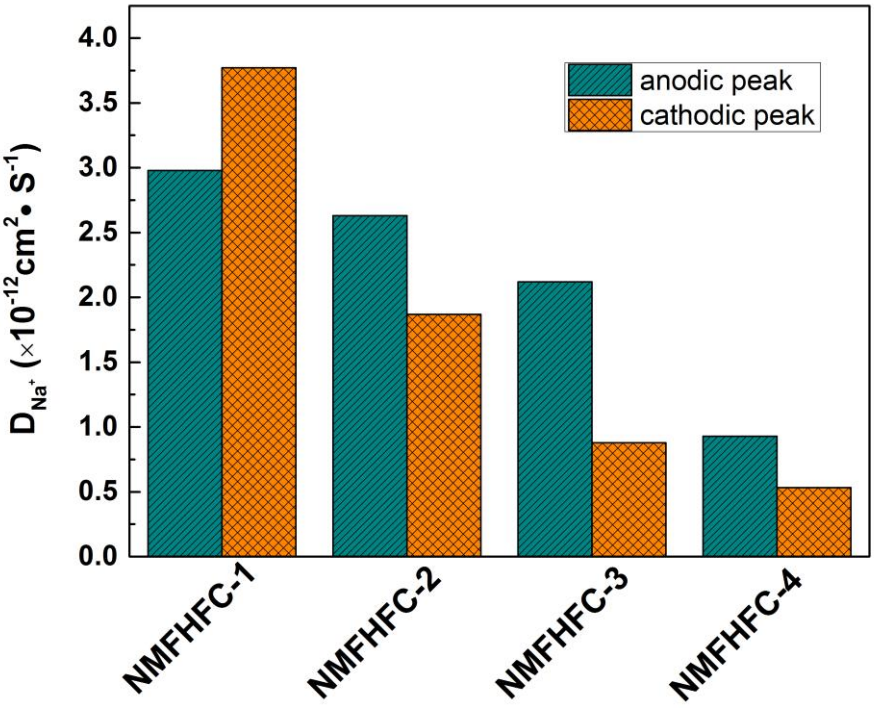

Figure S15. Diffusion coefficients of NMFHFC samples calculated from CV curves.

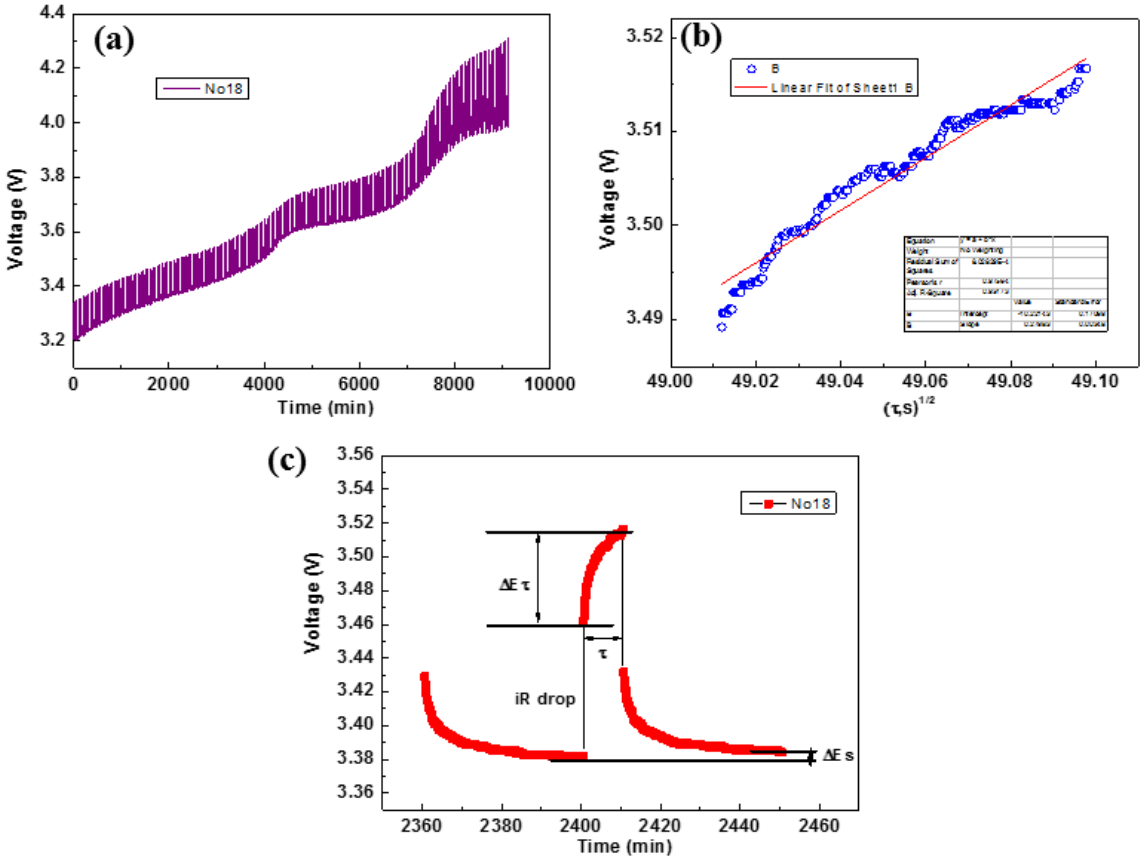

Figure S16. Galvanostatic intermittent titration technique (GITT) plots for NMFHFC-1: (a) GITT discharging curve during cycling as a function of time in the voltage range of 3.2-4.2 V.

(b) Plot of voltage vs. time ($\tau^{1/2}$) for the same titration to show the linear fit. (c) Voltage profiles before, during, and after a constant current pulse at 3.45 V, with schematic labelling of the different parameters.

Additionally, the galvanostatic intermittent titration technique (GITT) was also used to assess the diffusion coefficients of the NMFHFC samples in the charged states between 3.2-4.2 V. Figure S16 shows the galvanostatic intermittent titration technique (GITT) performance plots for the NMFHFC-1 sample. The cell is charged with a constant pulse for 10 minutes, followed by rest for 60 minutes, as shown in Figure S16(a). The Na^+ diffusion coefficient can be calculated according to Equation (2):[4]

$$D_{Na^+} = \frac{4}{\pi}\left(\frac{IV_m}{Z_A F A}\right)^2\left[\frac{dE(x)/dx}{dE(\tau)/d\sqrt{\tau}}\right]^2 \qquad (\tau \ll L^2/D_{Na^+}) \qquad (2),$$

Where I is the current applied (A), V_m is the molar volume of the electrode (cm^3/mol); Z_A is the charge number (for the Na ion battery, Z_A = 1), F is Faraday's constant, A is the electrode/electrolyte contact area (cm^2), $dE(x)/dx$ is the slope of the coulometric titration curve, $dE(\tau)/d\sqrt{\tau}$ is the slope of the linearized plot of the potential E (V) during the current pulse of duration τ (s), L (cm) is the characteristic length of electrode materials. If a sufficiently small current is used for short time intervals, so that $dE(\tau)/d\sqrt{\tau}$ can be considered linear and the coulometric titration curve ($dE(x)/dx$) can be also considered linear over the composition range involved in that step, Equation (2) can be simplified into Equation (3)[5]

$$D = \frac{4}{\pi\tau}\left(\frac{n_m V_m}{A}\right)^2\left(\frac{\Delta E_s}{\Delta E_\tau}\right)^2 \qquad (3),$$

in which, τ is the duration of the current pulse (s), n_m is the number of moles of host material (mol), V_m is the molar volume of the electrode (cm^3/mol), A is the electrode/electrolyte contact area (cm^2), ΔE_s is the steady-state voltage change due to the current pulse, and ΔE_τ is the voltage change during the constant current pulse, eliminating the iR drop. These parameters are illustrated in Figure S16(c).

Since the plot of the cell potential versus the square root of the duration time $\tau^{1/2}$ has a good linear fit (Figure S16(b)), the D_{Na^+} of the NMFHFC-1 composite can be calculated according to Equation (3), and it is found to be about $(0.4-11) \times 10^{-12}$ $cm^2 \cdot S^{-1}$ (Figure S17).

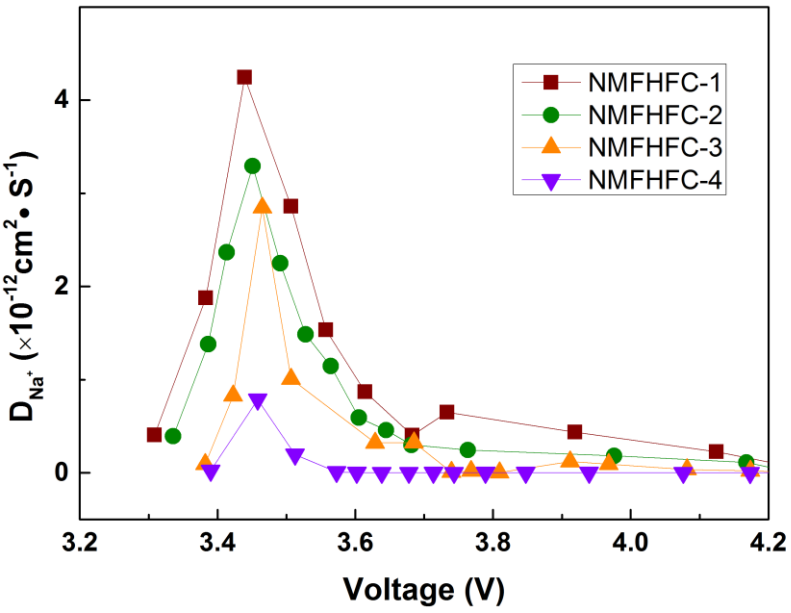

Figure S17. Comparison of Na^+ diffusion coefficients of NMFHFC samples calculated from GITT.

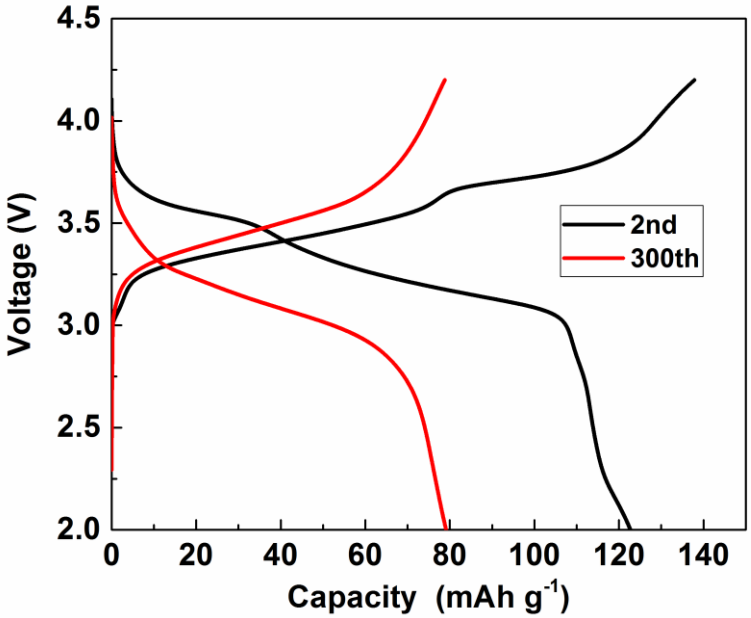

Figure S18. The charge-discharge curves of NMFHFC-1 at the 0.5 C rate after 300 cycle.

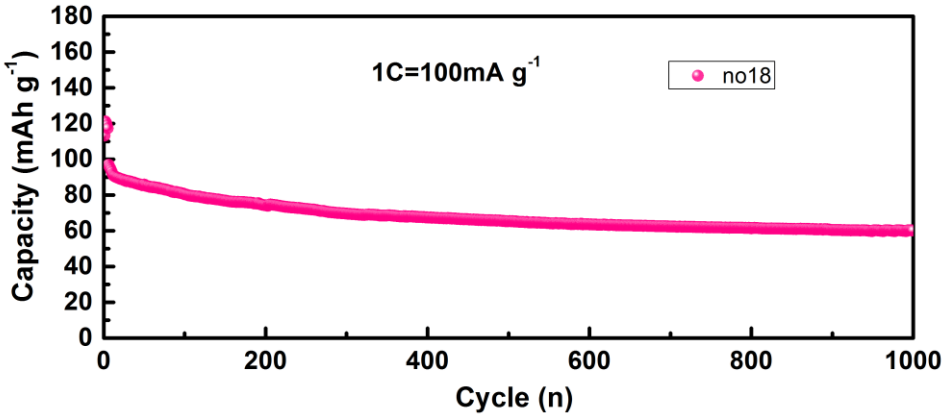

Figure S19. The cycling performance of NMFHFC-1 at the 1 C rate.

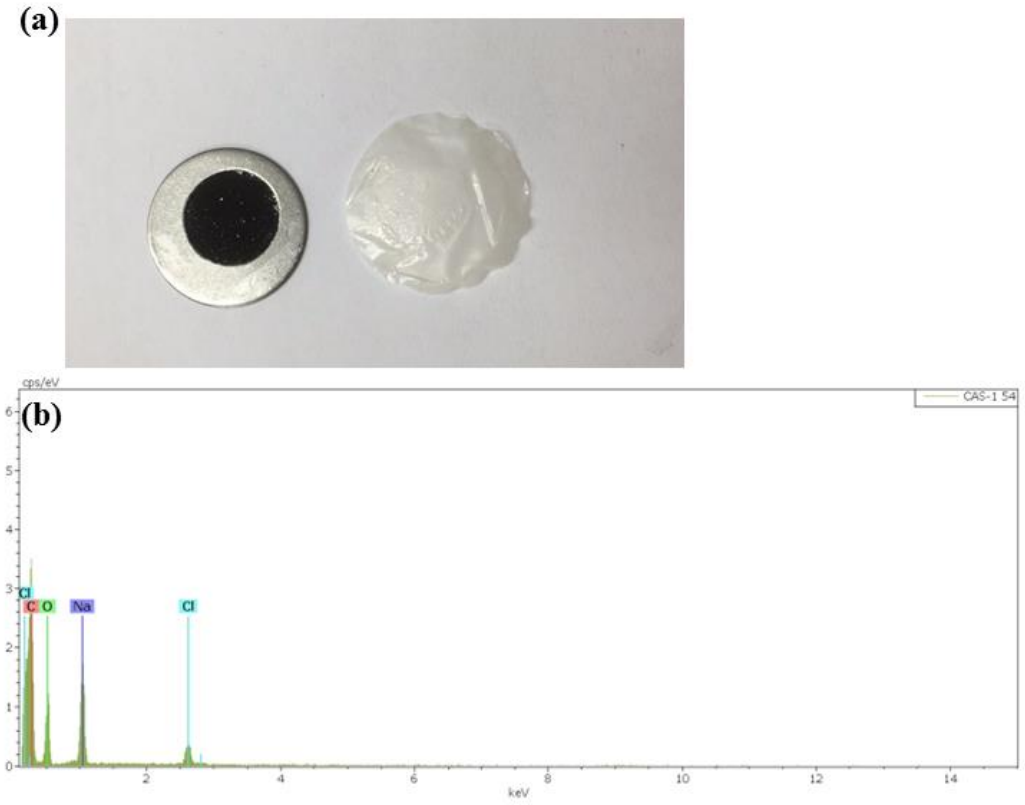

Figure S20. (a) Photograph and (b) EDS spectrum of the separator in the cell with NMFHFC-1 after 100 cycles.

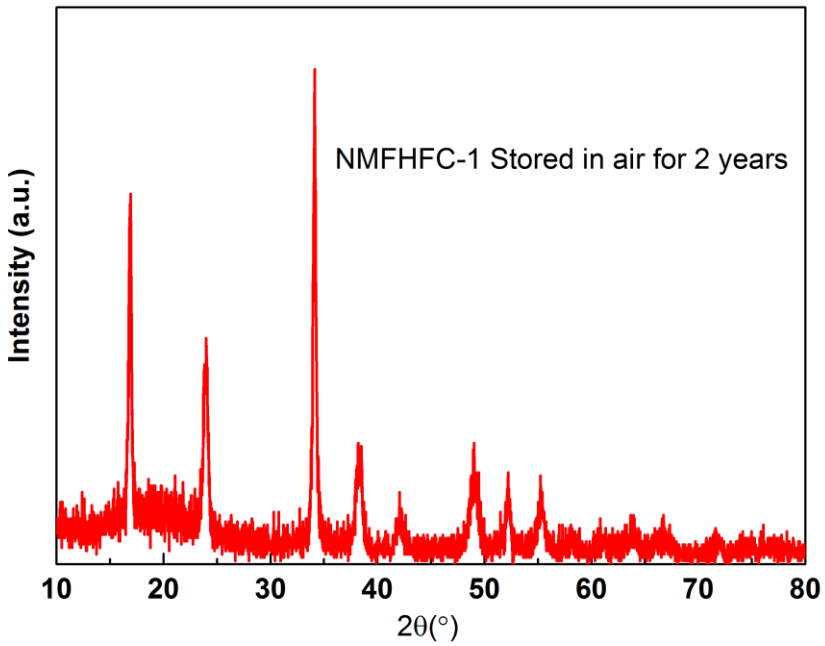

Figure S21. XRPD pattern of NMFHFC-1 stored under ambient atmosphere for 2 years.

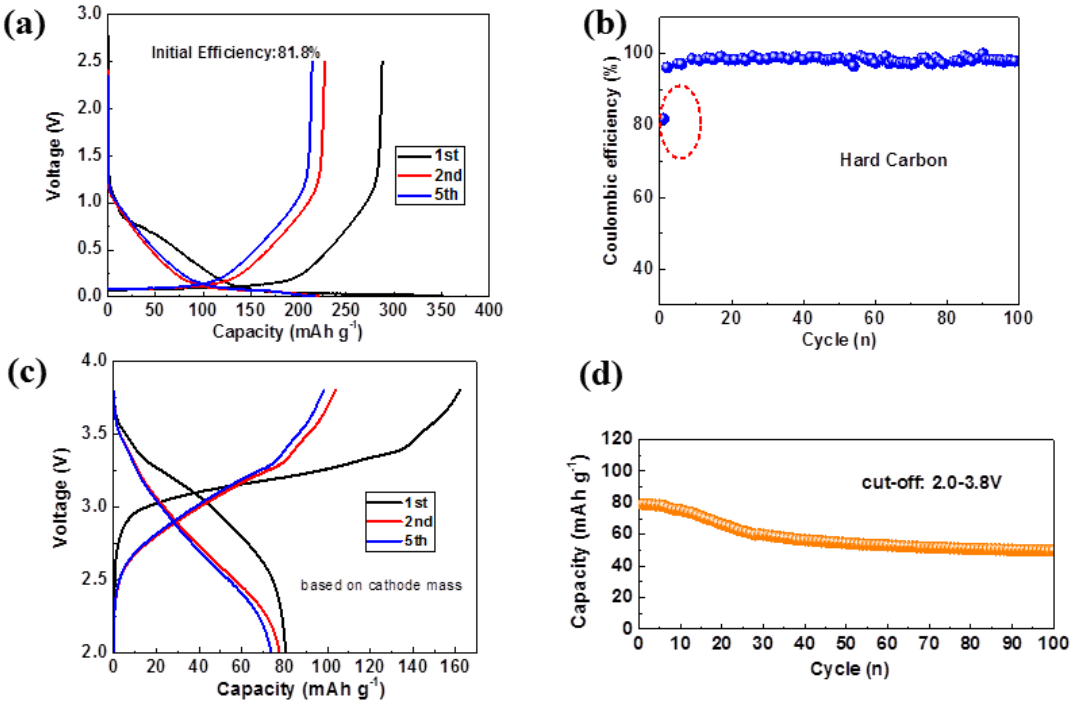

Figure S22. (a) charge-discharge curves and (b) coulombic efficiency of hard carbon, (c) the charge/discharge curves and (d) the cycling performance of NFMHFC-1/hard carbon full cell at voltage range of 2.0-3.8V.

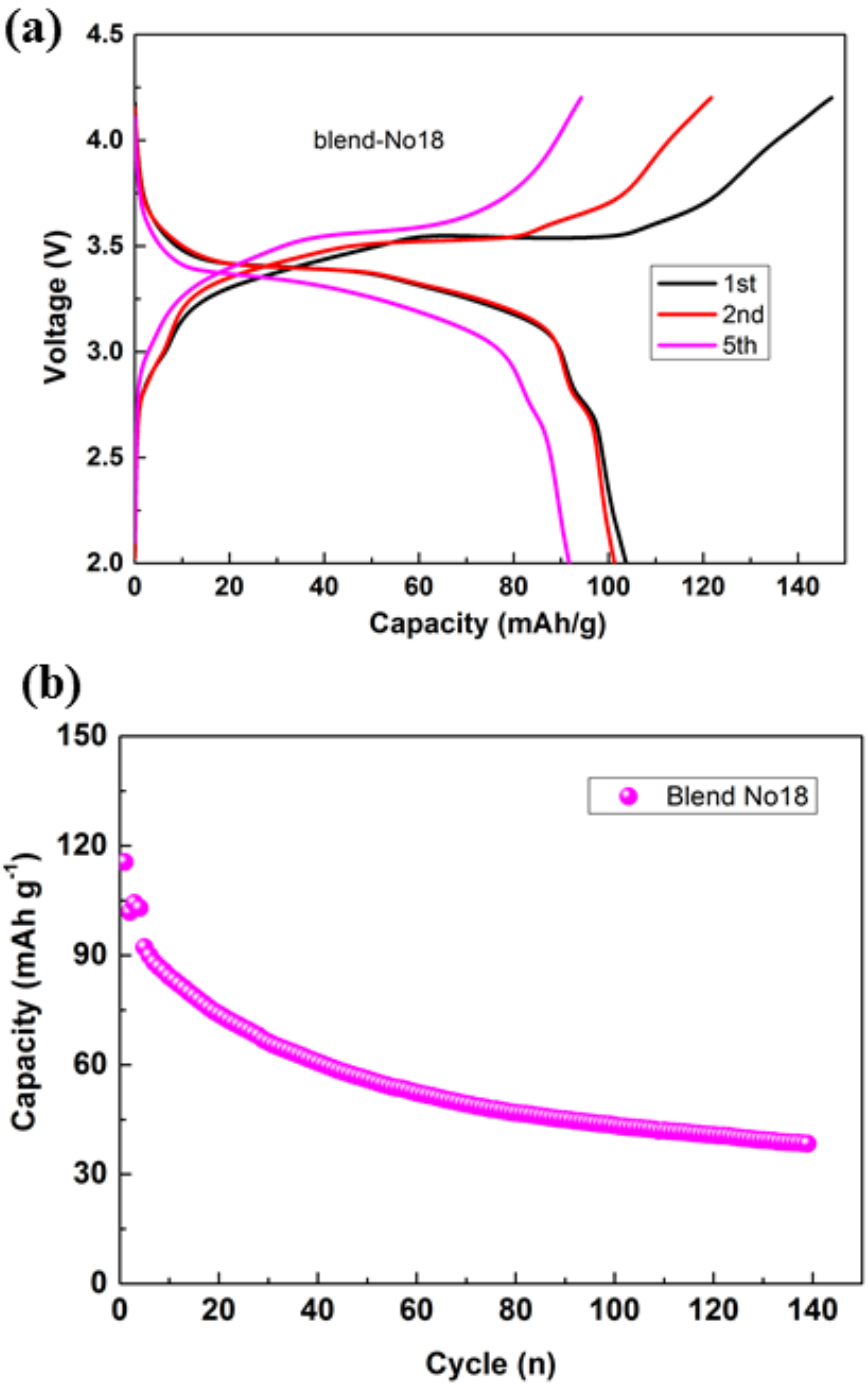

Figure S23. Electrochemical performance of B-NMFHFC-1: (a) charge-discharge curves, (b) cycling performance.

References

[1] L. Wang, Y. Lu, J. Liu, M. Xu, J. Cheng, D. Zhang, J. B. Goodenough, *Angewandte Chemie International Edition* **2013**, *52*, 1964-1967

[2] W. J. Li, S. L. Chou, J. Z. Wang, J. L. Wang, Q. F. Gu, H. K. Liu, S. X. Dou, *Nano Energy* **2015**, *13*, 200-207.

[3] J. Song, L. Wang, Y. Lu, J. Liu, B. Guo, P. Xiao, J. J. Lee, X. Q. Yang, G. Henkelman, J. B. Goodenough, *Journal of the American Chemical Society* **2015**, *137*, 2658-2664

[4] J. Wang, J. Polleux, J. Lim, B. Dunn, J. Phys. Chem. C 2007, 111, 14925-14931.

[5] Y. J. Zhu, C. S. Wang, *J. Phys. Chem. C* **2010**, *114*, 2830-2841.